Barred Galaxy Centres

EVIDENCE FOR INCREASED STAR FORMATION IN BARRED GALAXY CENTRES

BY JENNIFER M. LAING, B.SC., B.F.A.

A Thesis Submitted to the School of Graduate Studies
in Partial Fulfillment of the Requirements
for the Degree Master of Science

McMaster University

McMaster University
MASTER OF SCIENCE (2023)
Hamilton, Ontario, Canada (Physics and Astronomy)

TITLE:	Evidence for Increased Star Formation in Barred Galaxy Centres
AUTHOR:	Jennifer M. Laing B.Sc. (Astronomy and Astrophysics), University of Toronto, Toronto, Canada
SUPERVISOR:	Dr. Christine Wilson
NUMBER OF PAGES:	ix, 86

Abstract

Galactic bars play an important role in the dynamical evolution of their host galaxy, but their own evolution and impact on the local gas reservoir and star formation rate are still open questions. Recent work by the Physics at High Angular resolution in Nearby GalaxieS (PHANGS) collaboration found higher molecular gas surface densities and velocity dispersions in barred galaxies compared to unbarred galaxies. The higher turbulence found in bars is expected to create the observed increases. In this work, I explore bar turbulence in molecular gas using published high resolution measurements of CO$(2-1)$ from the PHANGS-ALMA survey. I compare properties of the molecular gas, such as surface density, velocity dispersion and star formation rate, in the centres of barred and unbarred galaxies. I consider the effect of galaxy environment on these properties from a local perspective (at cloud scales, $\approx$100 pc) for galaxies with and without an AGN. On global scales, I consider these properties in the context of the environment in which a galaxy lives, whether in a cluster or in the field. All three quantities (gas surface density, velocity dispersion, and star formation rate) are found to be enhanced in barred galaxy centres, even without an AGN and regardless of global environment.

Acknowledgements

First, I would like to thank my supervisor Dr. Christine Wilson for her help and guidance through this project. I am grateful for the opportunity to work in a field that has been a life long dream. Thank you for inspiring me and opening up new directions for research. I would also like to thank Dr. Jiayi Sun whose technical expertise and clear explanations of concepts have been extremely valuable.

Thank you also, to Blake for his continued patience with all of my questions, and to Hao, Celine, and Osvald for all of the helpful discussions. Thank you to Megan, Claude, and Taavishi for supportive chats and Starbucks breaks.

Finally, to my parents, Wes and Mary, and my sister Katherine, who have always encouraged and supported me and given me the incentive to keep going. Thank you for believing in me.

Table of Contents

List of Figures

List of Tables

Chapter 1

Introduction

The central region of a star forming galaxy is a dynamic place where physical processes interact on many scales. Some galaxy centres host structures such as a stellar bar or a star forming ring and studies have suggested that these local environmental structures play a role in the evolution of the galaxy (Kormendy and Kennicutt, 2004; Maeda et al., 2023). The star formation rate in different regions relates directly to the local physics; for example, star formation can be induced by shocks or stellar feedback or potentially suppressed by inflows of gas (Schinnerer et al., 2019).

On global scales, the evolution of galaxies and in particular the cold gas reservoir, has been shown to be influenced by the environment in which it lives (Boselli and Gavazzi, 2006; Cortese et al., 2021). Molecular gas properties on scales of giant molecular clouds (GMCs) where stars form in the cold molecular gas (Bolatto et al., 2008; Chevance et al., 2023) can give insight into how these galaxies evolve. My research explores the molecular gas in the central region of nearby galaxies, specifically comparing barred and unbarred galaxies.

1.1 Barred Galaxies

Star forming galaxies with a stellar bar are more common in the universe than unbarred galaxies, with over half of spiral galaxies showing a bar in images at optical and near infrared wavelengths (eg., de Vaucouleurs 1963; Díaz-García et al. 2020). Over the past few decades extensive observation and modeling work has revealed that barred galaxies have a dynamic structure that transports gas and stars and in so doing transforms the galaxy structure during its evolution (Jogee et al., 2004). Understanding the origin and formation of bars is still an active area of research.

Barred galaxies are known to have higher molecular gas surface densities in the central region than unbarred galaxies (Sheth et al., 2002b). We expect to find higher molecular gas surface densities in the centres because the bar structure drives an inflow of gas along the bar toward the centre of the galaxy (Sakamoto et al., 1999; Jogee et al., 2005; Díaz-García et al., 2021). This inflow of gas can fuel activity in the central nuclear region such as star formation in a circumnuclear ring or an active galactic nucleus (Sakamoto et al., 1999; Combes et al., 2019).

Velocity dispersion is also expected to be higher in the centres of barred galaxies because we expect there to be turbulence in bars and higher velocity dispersion indicates more turbulence. This relationship between the dynamics of the gas in the ISM and the star formation rate plays a key role in the evolution of galaxies (Krumholz, 2021). Gas dynamics as well as the properties of the gas vary in different regions of star forming galaxies – centres versus disks for example (Sun et al., 2020). In particular, galactic bars show complex physical processes, and a comparison of barred versus unbarred galaxies can give insight into which processes are dominant in bars.

Figure 1.1 shows NGC 3627, a spiral galaxy with a central bar. Denser regions

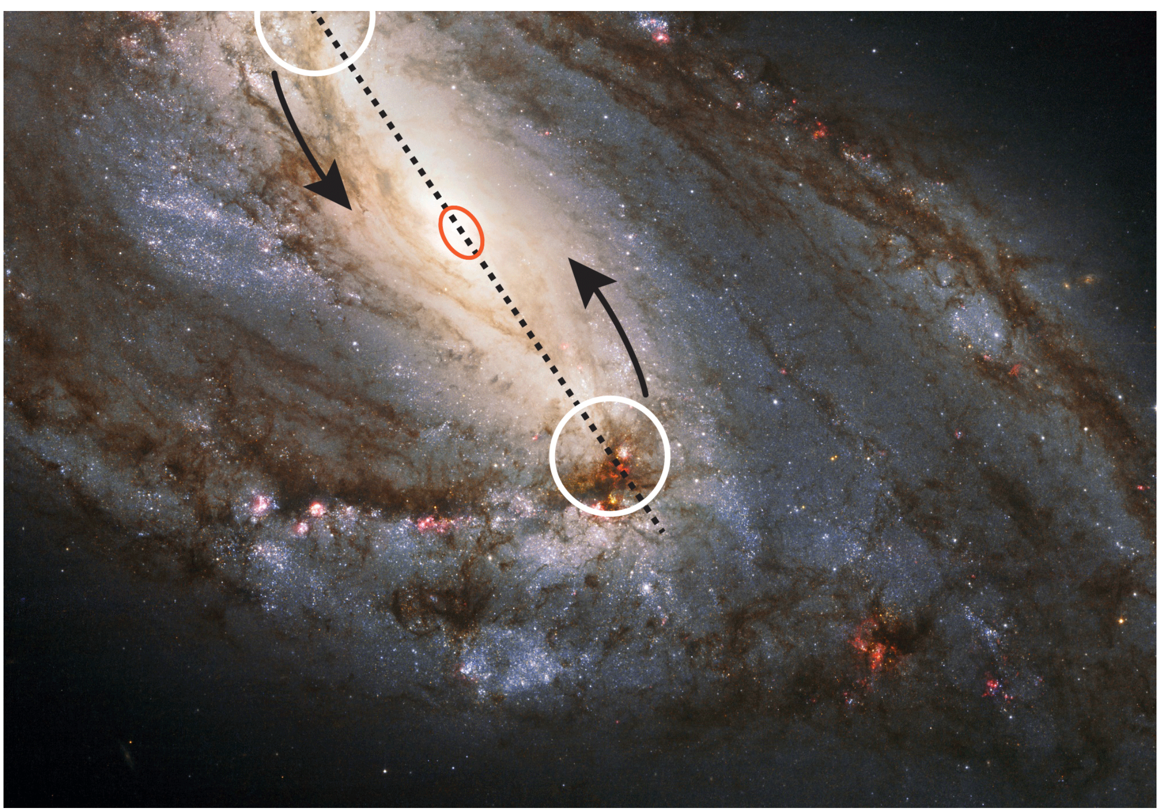

Figure 1.1 Hubble Space Telescope image of the barred spiral galaxy NGC 3627 in the Leo Triplet. The black dotted line indicates the axis of the bar. Gas piles up in the ends of the bar (white circles) leading to active star formation. Black arrows show radial inflow of gas along the bar and into the centre. The orange circle at the centre indicates the position (not to scale) of a star forming ring that could be present due to inflows of gas along the bar. (image credit: NASA/HST)

of active star formation occur at the ends and centre of the bar, while gas, stars and dust flow radially along the bar and turbulence is observed. This inflow of gas along the bar can cause intense star formation in a ring near the centre of the galaxy. An example of a galaxy where a central star forming ring is clearly seen is NGC 3351 in the Leo group (Regan et al., 2006).

The question of whether star formation is observed to be suppressed in bars is an active area of research. For statistical studies of a larger population of barred galaxies, the way that the bar is defined can produce different results. In a recent study, Maeda et al. (2023) do a statistical analysis of 18 nearby star forming barred galaxies and specify the various parts of the bar – the ends, centre, and along the length of the bar (Maeda et al., 2023). With the bar defined in this way they find that star formation is suppressed along the length of the bar, while there is more star formation in the ends and central region, as expected (Maeda et al., 2023). They specifically choose galaxies with a gas-rich, long-bar structure. If the bar is instead defined as one entity that encloses all three parts of the bar then the gas and star formation measurements are mixed together and can show increases in these properties for the whole bar (Querejeta et al., 2021; Díaz-García et al., 2021). This second method of selection often cannot be avoided due to the resolution of the data and distance to galaxies.

1.2 Molecular Gas in Galaxies

While the atomic gas in galaxies can extend out past the galactic disk, molecular gas in galaxies is generally more concentrated towards the inner 10 kpc of the galaxy (Brown et al., 2021). Stars form inside clouds of molecular gas comprising mainly molecular hydrogen (H_2), the most abundant molecule. The production and destruction of these giant molecular clouds (GMCs) informs us about the star formation rate in galaxies and understanding where this occurs can give insight about how different structures in a galaxy evolve (McKee and Ostriker, 2007; Bolatto et al., 2008; Chevance et al., 2023). These clouds require low temperatures ($\sim$10 K) to begin to collapse to form stars; however, at these temperatures H_2 is not possible to detect because the molecule has a very low mass, which is only excited to higher energy states at higher temperatures (Habart et al., 2005; Kennicutt and Evans, 2012). Instead, carbon monoxide (CO) is used as a tracer of molecular gas because it has strong emission lines and often lives in the same space as H_2 (Kennicutt and Evans, 2012; Leroy et al., 2013b). The CO transition $J = 1 \rightarrow 0$, hearafter CO$(1-0)$ occurs at a wavelength of 2.6 mm and falls within Earth's atmospheric window and so can be observed by telescopes on the ground (Bolatto et al., 2013). CO is quite optically thick, so it is used alongside the CO isotopes ^{13}CO and C^{18}O to reach different optical depths in GMCs and therefore determine a column density for the molecular gas in the cloud (Kennicutt and Evans, 2012).

Because the molecule we really want to measure is H_2, the integrated intensity of CO (in units of K km s^{-1}) is converted to an estimate of the surface density, Σ, of H_2 using a conversion factor α_{CO}, which has units of $M_\odot$ pc^{-2} (K km s^{-1})$^{-1}$. The calculation for α_{CO} has been done in different ways, often taking metal abundance into account (Bolatto et al., 2013). At low metallicity CO emission can be faint, even for actively star forming galaxies, so we expect metallicity to be an important factor in the value of α_{CO} (Bolatto et al., 2013). Several rotational emission lines of CO are commonly observed, CO$(1-0)$, CO$(2-1)$, and CO$(3-2)$, and α_{CO} is derived for each of them (Bolatto et al., 2013; Sun et al., 2018). In addition to α_{CO}, the estimate of H_2 also factors in the line ratio between $CO(1-0)$ and the emission line being studied. Extensive work has been to done to determine the optimal value for α_{CO} and the line ratios (eg., Bolatto et al. 2013; Maeda et al. 2022). The conventions adopted for my work are explained in Chapter 2.

Several surveys tracing CO in nearby galaxies are available now from the Atacama Large Millimeter/Sub-millimeter Array (ALMA) and can be used to measure the gas at various scales. ALMA, located in the Chilean Andes, is an interferometer made up of 66 antennas, fifty-four 12 m and twelve 7 m antennas in different configurations, spread over 16 km in the Atacama region. The large baseline allows measurements to reach high resolution within extra galactic sources. Data collected from each antenna in the array are all combined together to create a high resolution product in the form of a spectral cube. Each cube has two spatial dimensions and a third spectral dimension. ALMA observes at wavelengths between infrared and radio ($0.32-3.6$ mm), making it ideal for studies of molecular gas which peak in this part of the spectrum. (source: https://www.eso.org/public/teles-instr/alma/)

One example of a recent survey is by the Physics at High Angular resolution in Nearby GalaxieS (PHANGS) collaboration, which forms the basis for my work. PHANGS-ALMA is a survey of resolved molecular gas which reaches high precision within nearby (<50 Mpc) galaxies (Leroy et al., 2021b). The spatial scale is ∼100 pc which corresponds to the size of a GMC. Figure 1.2 shows the precision of the observations of PHANGS for one of the galaxies in the survey NGC 3627 (Rosolowsky et al., 2021). The image shows the integrated intensity map of the $CO(2-1)$ emission with highlighted regions placed on top. Each of the red ellipses in the image is one

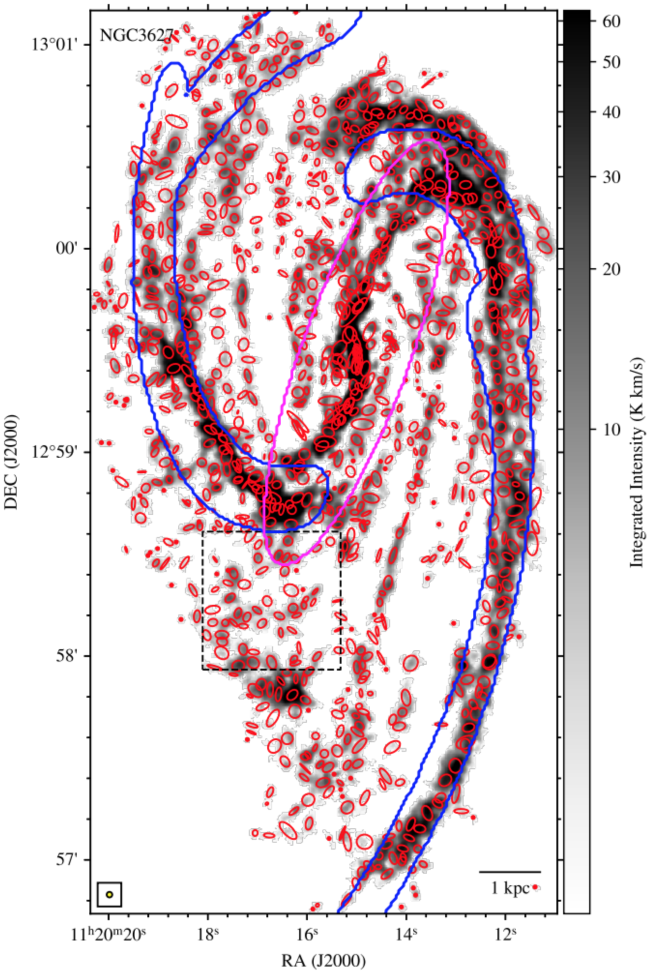

Figure 1.2 The integrated intensity map of the CO(2 − 1) emission in NGC 3627. GMCs are highlighted with red ellipses, the galactic bar is circled in pink, and the galactic arms are outlined in blue. GMCs are concentrated in the central region and in the arms (Rosolowsky et al., 2021). (image credit: PHANGS-ALMA)

GMC. The bar in this galaxy is circled in pink and the galactic arms are outlined in blue. We see the concentration of GMCs in the central region.

1.3 Star Formation in Galaxies

Change to the star formation activity in a galaxy is one of the main ways we can observe galaxy evolution. Understanding where star formation occurs and the rate at which it is happening can reveal information about the dynamics of the region and other physical mechanisms at play (eg., Kennicutt and Evans 2012). In a resolved study of the molecular gas and star formation in four barred galaxies, Sheth et al. (2002a) found that the star formation is highest along the leading edge of the stellar bar, giving insight into the rotation and dynamics of the galactic bar.

The rate of star formation in galaxies is found by using a combination of multiple wavelengths and emission lines to give a relatively complete picture of the stars in a given region. Hα traces the ionized gas around massive stars ($\geq$10 $M_\odot$) with short lifetimes, which traces star formation in the last $\sim$20 Myrs (Kennicutt, 1989). Far-ultraviolet (FUV) and near-ultraviolet (NUV) probe emission from young stars of a few solar masses, tracing stars that would have formed within 100 Myrs (FUV) and 200 Myrs (NUV) (Kennicutt and Evans, 2012). Infrared (IR) observations which span wavelengths in the range of $(3.6-500)$ μm, detect light that has been re-emitted by dust after having been absorbed, so IR provides measurements of stars that are obscured by dust at shorter wavelengths (Kennicutt and Evans, 2012). Like FUV, IR traces stars that are in the range of 100 Myrs old (Kennicutt and Evans, 2012).

There has been a giant leap forward in recent years in the ability to study star formation in galaxies due to advances in technology such as the Galaxy Evolution Explorer (GALEX) and the Wide-Field Infrared Survey Explorer (WISE). The GALEX mission (Martin et al., 2005) collected UV data across the sky in FUV ($\sim$154 nm) and NUV ($\sim$231 nm) (Leroy et al., 2019). The WISE mission (Wright et al., 2010) traced the IR sky at four IR wavelengths, 3.4, 4.5, 12, and 22 μm (Leroy et al., 2019). Both of these missions along with the Sloan Digital Sky Survey (SDSS) have made it possible to study star formation for large samples of galaxies at a time. Using GALEX and WISE images for $\sim$15,000 galaxies Leroy et al. (2019) was able to publish an altas of galaxies at UV and IR wavelengths that has been widely used as a standard for star formation rates. One recent study looks at over 700 barred galaxies selected from the SDSS with complementary UV data from GALEX as well as Hα images and they are able to distinguish spatial distributions of star formation in bars, identifying regions such as the circumnuclear region and bar ends where star formation is higher (Díaz-García et al., 2020).

The well known Kennicutt-Schmidt (KS) relation compares the star formation rate surface density, $\Sigma_{\rm SFR}$, with the surface density of the gas. Early versions of this relation used the total gas $-$ atomic hydrogen, HI, and molecular hydrogen, H_2 (Kennicutt and Evans, 2012), but it has become more common to make the comparison with the surface density of the molecular gas, $\Sigma_{\rm H_2}$:

$$\Sigma_{\rm SFR} \propto \Sigma_{\rm H_2}^{N}, \tag{1.3.1}$$

with power law index N (Jiménez-Donaire et al., 2023). Using H_2 for the comparison is reasonable and makes sense physically given that stars form in cold H_2 regions.

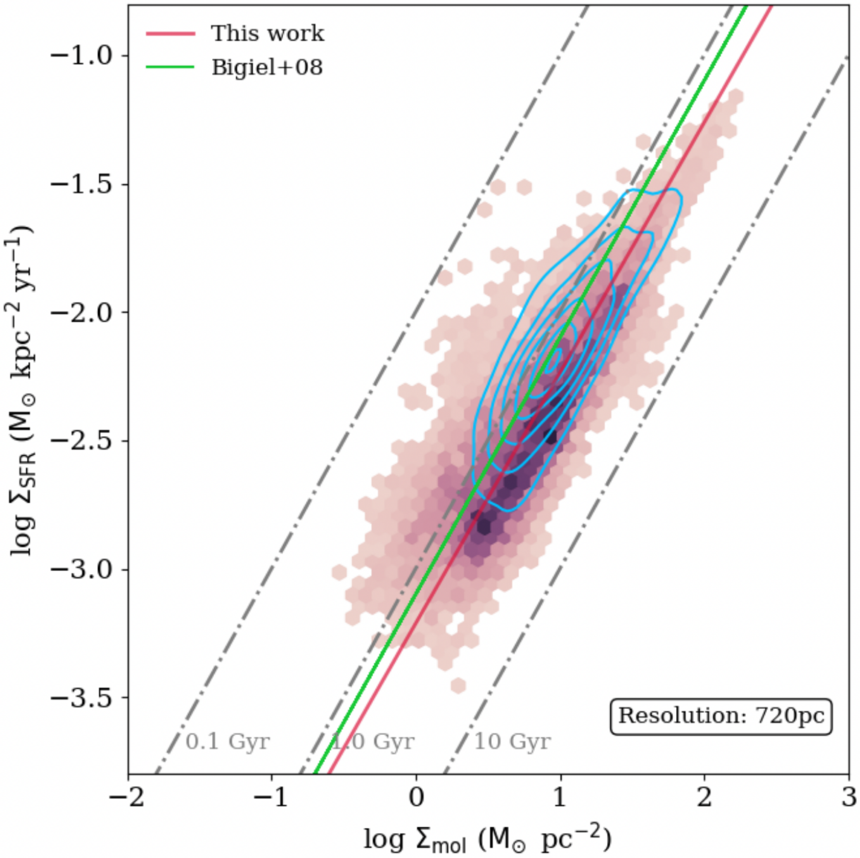

Figure 1.3 The resolved Kennicutt-Schmidt relation for VERTICO (Virgo Environment Traced in CO) galaxies at 720 pc resolution by Jiménez-Donaire et al. (2023) [pink]. The best fit line for the K-S relation is shown in dark pink and compared to another resolved study by Bigiel et al. (2008) in green. The dashed lines show constant depletion times (the ratio of the two quantities, $t_{\rm dep} = \Sigma_{\rm mol}/\Sigma_{\rm SFR}$). The blue contours represent another resolved sample of galaxies from the HERACLES (HERA CO-Line Extra-galactic Survey) used as a comparison. Image credit: VERTICO, Jiménez-Donaire et al. (2023).

The KS relation for global galaxy measurements shows a strong positive correlation and many studies have found a power law index in the range found originally by Kennicutt (1989), $N = 1.40 \pm 0.15$. Recently, as many large surveys of resolved data have become available the KS relation has been analysed again in the resolved context. Jiménez-Donaire et al. (2023) study data from the Virgo Environment Traced in CO (VERTICO) survey of resolved molecular gas for 51 galaxies in the Virgo Cluster. Figure 1.3 shows the results for the resolved KS relation; the resulting slope is shown in pink (0.97 ± 0.07) for all of the galaxies at 720 pc resolution, and compared to results from another resolved study in green. Dashed lines show constant depletion times (the ratio of the two quantities, $t_{\rm dep} = \Sigma_{\rm mol}/\Sigma_{\rm SFR}$). They find that there can be varying slopes (within a range of $0.69 - 1.40$) for the KS relation for individual galaxies in the sample (Jiménez-Donaire et al., 2023).

1.4 Turbulence

Observations of the turbulence in galaxies have been made possible with more resolved observations of nearby (<50 Mpc) star forming barred galaxies. The centres of these galaxies have been shown to have higher velocity dispersion (σ_v), and molecular gas surface densities than the unbarred galaxy centres as well as the rest of the spiral disks (Sun et al., 2020; Krumholz, 2021). A higher velocity dispersion means more turbulence in the gas.

Star formation, as discussed, happens inside dense clouds of molecular gas, and can be enhanced or disrupted depending on the presence of turbulence in and around the cloud (Krumholz, 2021). Turbulence makes up a significant fraction of the energy balance in molecular clouds and has been shown to be more important than rotation, and equally, or more important, than magnetic energy (Heyer and Brunt, 2007). As such, it may be the main process holding up the clouds from collapsing catastrophically to form stars.

The source of the driving mechanism causing the turbulence is an ongoing question. There are two suggested theories as to the source of turbulence in the gas (Krumholz et al., 2018). The first is that it originates from stellar feedback in the form of supernovae, jets from protostellar disks or stellar winds. The second mechanism is from inflows of gas along a bar or from an external origin. Observational studies have proposed that stellar feedback cannot be the only source of turbulence, but that inflows could be the main mechanism responsible for increased velocity dispersions in disks or in more extreme environments like starbursts or mergers (Krumholz et al., 2018; Brunetti et al., 2021). Bars also suppress star formation (Maeda et al., 2023) which would cause there to be less stellar feedback. In that case we would expect a decrease in turbulence.

1.5 Active galactic nuclei

The centres of galaxies with an active galactic nucleus (AGN) can show inceases in molecular gas surface density and velocity dispersion (Stuber et al., 2021; Combes et al., 2019). AGN are bright compact objects that can be fuelled by gas inflows along a stellar bar in the centre of the galaxy (Sakamoto et al., 1999). At the same time, observations have shown that AGN can produce galactic outflows that push molecular gas out of the galaxy, effectively shutting down star formation (Stuber et al., 2021). However, outflows can also enhance star formation through gas compression induced by shocks (Maiolino et al., 2017). The exchange of gas in the centre of galaxies through inflows and outflows plays an important role in regulating star formation in this region (Combes, 2019; Stuber et al., 2021).

1.6 Environment

The external environment can also alter the galaxy's gas content. Galaxies in the extreme environment of a cluster of galaxies have less gas to form stars and thus less star formation (Haynes and Giovanelli, 1984; Cortese et al., 2011; Brown et al., 2021).

Inside a dense environment such as the Virgo Cluster, the medium between the galaxies is heated up as a result of the cluster's massive gravitational potential. In these regions, 1000s of galaxies are moving past each other at velocities of up to thousands of kilometres per second (eg., Brown et al. 2021). Galaxies moving through this hot medium will lose gas through ram pressure stripping (RPS), as demonstrated in Figure 1.4 for a galaxy in the Virgo Cluster. The galaxy is inclined along the line of sight, and as it moves down and to the left in the image, gas is drawn out of the galaxy through strong winds. This gas removal can quench galaxies and stop them forming stars. Extensive observational and theoretical studies have confirmed this large scale physics (eg., Boselli and Gavazzi 2006).

Studies of how the environment affects star formation in galaxies have been done for decades. For example, Koopmann and Kenney (2004) used Hα observations of massive stars to study the massive star formation rate in Virgo Cluster galaxies compared with isolated galaxies, and found truncated radial profiles for galaxies in the Virgo Cluster.

Star formation happens inside dense clouds of molecular gas, on much smaller scales (<100 pc) than the $10^4 - 10^6$ pc scale of galaxies and clusters. Measurements

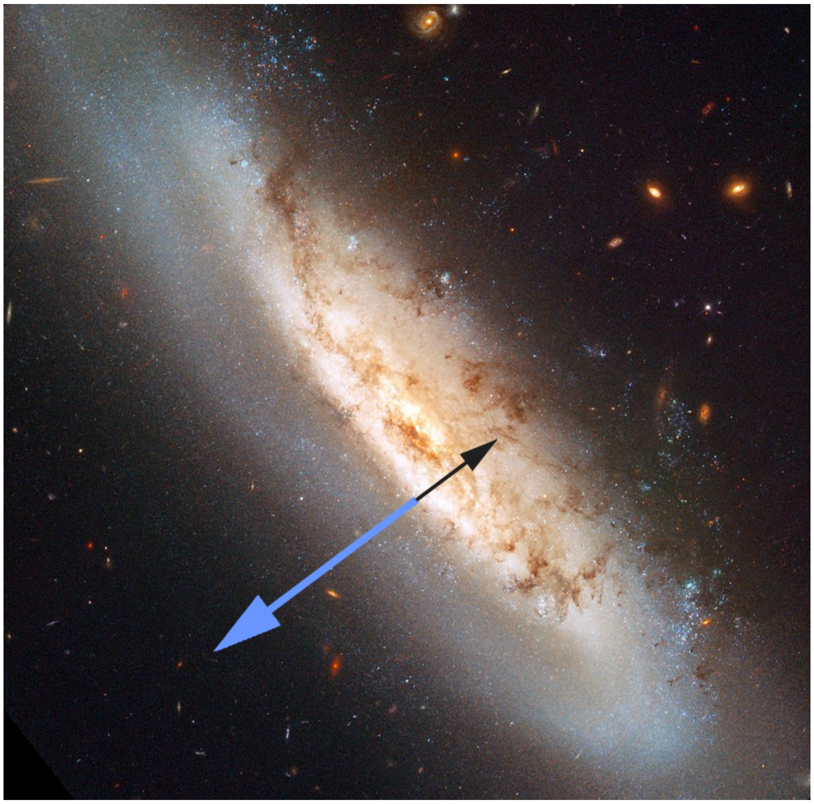

Figure 1.4 Hubble Space Telescope (HST) image of the spiral galaxy NGC 4522 in the Virgo cluster. The blue arrow points in the direction of motion of the galaxy while the black arrow points towards swirls of gas and dust being stripped out of the galaxy as it moves at extreme velocities (10^3 km/s) through the hot intergalactic medium in the cluster, through a process called ram pressure stripping. Credit: NASA/ESA

of the molecular gas surface density (Σ_{mol}), velocity dispersion (σ_v), virial parameter (α_{vir}), and internal gas pressure trace the cloud-scale physics. Molecular clouds can be disrupted by physical processes such as increased turbulence in and around the cloud. On global scales I consider these properties in the context of the environment in which a galaxy lives, whether in a cluster or in the field.

1.7 This Thesis

This research is motivated by recent work by the PHANGS collaboration. Sun et al. (2020) showed higher molecular gas surface density and velocity dispersion for the centres of barred galaxies compared to unbarred galaxies. Higher velocity dispersion can indicate more turbulence in the gas, impacting star formation which will affect the evolution of the galaxy. Querejeta et al. (2021), also in the PHANGS collaboration, explored several properties in different regions of the galaxies in the sample. Results from these two papers suggested that there was scope to do further work specifically looking at the central region.

I am comparing the gas properties such as molecular gas surface density, velocity dispersion and star formation rate to understand how these quantities differ in the central region between barred and unbarred galaxies. Velocity dispersion and molecular gas surface density are straight forward to measure from observations and together tell us how turbulent motions scale with the gas surface density. Detailed region masks have been created for the PHANGS galaxies (Querejeta et al., 2021). I have explored different ways of defining the central region, such as the central 1 kpc, or a percentage of the effective radius of each galaxy to determine what effect the definition of centre has on the results.

In Chapter 2 I describe the data and reduction techniques used as well as the statistical analysis that was conducted. In Chapter 3 I discuss the results of the analysis. In Chapter 4 I present some conclusions and future work prospects.

Chapter 2

Sample and Data Products

2.1 PHANGS-ALMA sample

My research uses published CO$(2-1)$ data from the PHANGS-ALMA survey of nearby star forming galaxies at cloud scale resolutions of < 150 pc (Sun et al., 2018, 2020; Leroy et al., 2021b). In total, my sample consists of 64 galaxies, with 61 galaxies from the PHANGS-ALMA Large Program and 3 galaxies from an extended sample observed for PHANGS-ALMA (extended sample described on page 19). The full PHANGS-ALMA Large Program is described in Leroy et al. (2021b). It consists of 90 galaxies in total with 75 in the main sample, and an additional 15 galaxies in the extended sample. I will explore including these additional galaxies in my future work. In this chapter I describe some key aspects of the sample and data products, and I begin by outlining the PHANGS-ALMA sample selection process which is explained in detail in Leroy et al. (2021b).

Galaxies in the PHANGS-ALMA Large Program sample were intended to meet the following criteria:

- Distance: One of the main science goals for the survey was to study resolved GMCs inside galaxies. To achieve this, targets needed to be close enough that one arcsec on the sky equals less than a physical length of 100 pc ($1'' \leq 100$ pc). Therefore the original distance limit was $d < 17$ Mpc.
- Inclination: Galaxies with lower inclination allow individual GMCs to be separated from others, so an inclination cut of $i < 75^\circ$ was implemented.
- Declination: Galaxies needed to be visible from the southern hemisphere where ALMA is located, so the declination range was $-75^\circ < \delta < +25^\circ$.
- Mass: Galaxies needed to have a stellar mass of $\log_{10}$ M$_*$ [M$_\odot$] ≥ 9.75, which is relatively massive. As indicated in Leroy et al. (2021b), this was to avoid low-mass galaxies where the metallicity can be low and CO can be difficult to detect compared with more massive galaxies (Bolatto et al., 2013; Hunt et al., 2015; Schruba et al., 2017). This mass threshold represents masses greater than twice the mass of dwarf galaxies such as the LMC. My final sample has global stellar masses within the range $10^{9.27} - 10^{11.15}$ M$_\odot$.
- Star formation rate: Galaxies needed to be actively forming stars with a specific SFR (sSFR) = SFR/M$_* > 10^{-11}$ yr^{-1}. The sSFR is the SFR relative to the stellar mass of the galaxy (Blanton and Moustakas, 2009). This threshold removes galaxies with a low sSFR that are no longer forming stars, but keeps galaxies with high sSFR values such as starbursts. However, there are not many starbursts in the sample since these are most often located at distances farther than 17 Mpc.

All galaxies in the main sample met the criteria above with some uncertainties.

The extended sample represents galaxies that do not necessarily meet all of the criteria, or which were missed in the PHANGS-ALMA initial selection (Leroy et al., 2021b). The accepted distance to galaxies in the Virgo cluster is 16.5 Mpc (Ferrarese et al., 2012), so most of the sample represents galaxies within that distance.

Galaxies in my sample are shown in Table 2.1, where the columns show the classifications used in my research. I give a designation of barred or unbarred for all galaxies in the sample. To classify a galaxy as barred I match the classification given in Sun et al. (2020), or if it is unknown in that paper I follow Stuber et al. (2021). All other galaxies are given the designation unbarred. I also follow Stuber et al. (2021) for the classification of whether the galaxy has an AGN in the centre or not. I use the NASA/IPAC Extragalactic Database (NED) to identify the galactic environment, and in the description column I have indicated if a galaxy is isolated, in a group or pair, or is part of a cluster. For my analysis I have bundled all galaxies that are not in a cluster and refer to these as field galaxies, or galaxies not in a cluster. If NED did not give a designation I treat those as isolated galaxies. The three galaxies that are from the PHANGS-ALMA extended sample are ESO097-013 (Circinus), NGC 0253, and NGC 0300.

Table 2.1: Galaxy list

Galaxy	**Bar**	**AGN**	**Cluster**	**Description**
ESO097-013	N	Y	N	Isolated
IC1954	Y	N	N	Group
IC5273	Y	N	N	Group (Sculptor)
NGC0253	Y	Y	N	Group (Sculptor)

Continued on the next page

Continued from previous page

Table 2.1: Galaxy list continued

Galaxy	**Bar**	**AGN**	**Cluster**	**Description**
NGC0300	N	N	N	Group (Sculptor)
NGC0628	N	N	N	Isolated
NGC0685	Y	N	N	Pair Member
NGC1087	Y	N	N	Group
NGC1097	Y	Y	N	Group
NGC1300	Y	N	Y	Cluster (Eridanus)
NGC1317	Y	N	Y	Cluster (Fornax)
NGC1365	Y	Y	Y	Cluster (Fornax)
NGC1385	N	N	Y	Cluster (Eridanus)
NGC1433	Y	N	N	Group
NGC1511	N	N	N	Group
NGC1512	Y	N	N	Group
NGC1546	N	N	N	Group (Dorado)
NGC1559	Y	N	N	Group (Dorado)
NGC1566	Y	Y	N	Group (Dorado)
NGC1637	Y	N	N	-
NGC1792	N	N	N	Group
NGC2090	N	N	N	-
NGC2283	Y	N	N	Pair Member
NGC2566	Y	N	N	Group

Continued on the next page

Continued from previous page

Table 2.1: Galaxy list continued

Galaxy	**Bar**	**AGN**	**Cluster**	**Description**
NGC2835	Y	N	N	Group
NGC2903	Y	N	N	Isolated
NGC2997	N	N	N	Group
NGC3137	N	N	N	Group
NGC3351	Y	N	N	Group (Leo)
NGC3507	Y	N	N	Group
NGC3511	Y	N	N	Pair Member
NGC3521	N	N	N	Isolated
NGC3596	N	N	N	Isolated
NGC3621	N	Y	N	Isolated
NGC3626	Y	N	N	Group
NGC3627	Y	Y	N	Group
NGC4254	N	N	Y	Cluster (Virgo)
NGC4293	Y	N	Y	Cluster (Virgo)
NGC4298	N	N	Y	Cluster (Virgo)
NGC4303	Y	Y	Y	Cluster (Virgo)
NGC4321	Y	N	Y	Cluster (Virgo)
NGC4457	Y	Y	Y	Cluster (Virgo)
NGC4496A	Y	-	Y	Cluster (Virgo)
NGC4535	Y	N	Y	Cluster (Virgo)

Continued on the next page

Continued from previous page

Table 2.1: Galaxy list continued

Galaxy	**Bar**	**AGN**	**Cluster**	**Description**
NGC4536	Y	N	Y	Cluster (Virgo)
NGC4540	Y	N	Y	Cluster (Virgo)
NGC4548	Y	Y	Y	Cluster (Virgo)
NGC4569	Y	Y	Y	Cluster (Virgo)
NGC4571	N	N	Y	Cluster (Virgo)
NGC4689	N	N	Y	Cluster (Virgo)
NGC4731	Y	N	N	Group (Virgo Y)
NGC4781	Y	N	N	Group
NGC4826	N	Y	N	Isolated
NGC4941	Y	Y	N	Group
NGC4951	N	N	N	Group
NGC5042	N	N	N	-
NGC5068	Y	N	N	Group
NGC5134	Y	N	N	Group
NGC5248	Y	N	N	Isolated
NGC5530	N	N	N	-
NGC5643	Y	Y	N	-
NGC6300	Y	Y	N	Group
NGC7456	N	N	N	Group
NGC7496	Y	Y	N	Group

2.2 Data and conversion to physical quantities

My analysis uses data products compiled by members of the PHANGS collaboration taken from Leroy et al. (2021a,b), Sun et al. (2018, 2020, 2022), and Querejeta et al. (2021). I summarize the data characteristics of the observed quantities and conversion to physical quantities below.

The raw data from the PHANGS-ALMA CO$(2-1)$ survey come from ALMA observations using the 12 m and 7 m interferometric arrays as well as single-dish measurements that are combined together (Leroy et al., 2021a,b). Measurements using ALMA interferometry are provided in the form of a data cube, where each cube has two spatial dimensions and a third spectral dimension. The spectral axis can be collapsed down by integrating over the intensity in order to create two dimensional image maps for the "moments" of the spectrum, where the zeroth moment is the integrated intensity (I_{CO}), the first moment is the mean velocity field and the second moment is the spectral line width or velocity dispersion (σ_v) along the line of sight.

Combining interferometric and single dish measurements for PHANGS-ALMA makes it possible to access emission from the full range of spatial scales above 50 to 150 pc. Since the 64 galaxies in the sample range in both size and distance, the data cubes for each galaxy were convolved to 150 pc resolution for consistency across the sample (Leroy et al., 2021b). The image maps created for I_{CO} and σ_v have a high resolution where each pixel in the image represents one sightline and is the approximate size of a molecular gas cloud. Figure 2.1 shows I_{CO} maps for two galaxies in the sample, one barred (NGC 3627) and one unbarred (NGC 4254) from Leroy et al. (2021a).

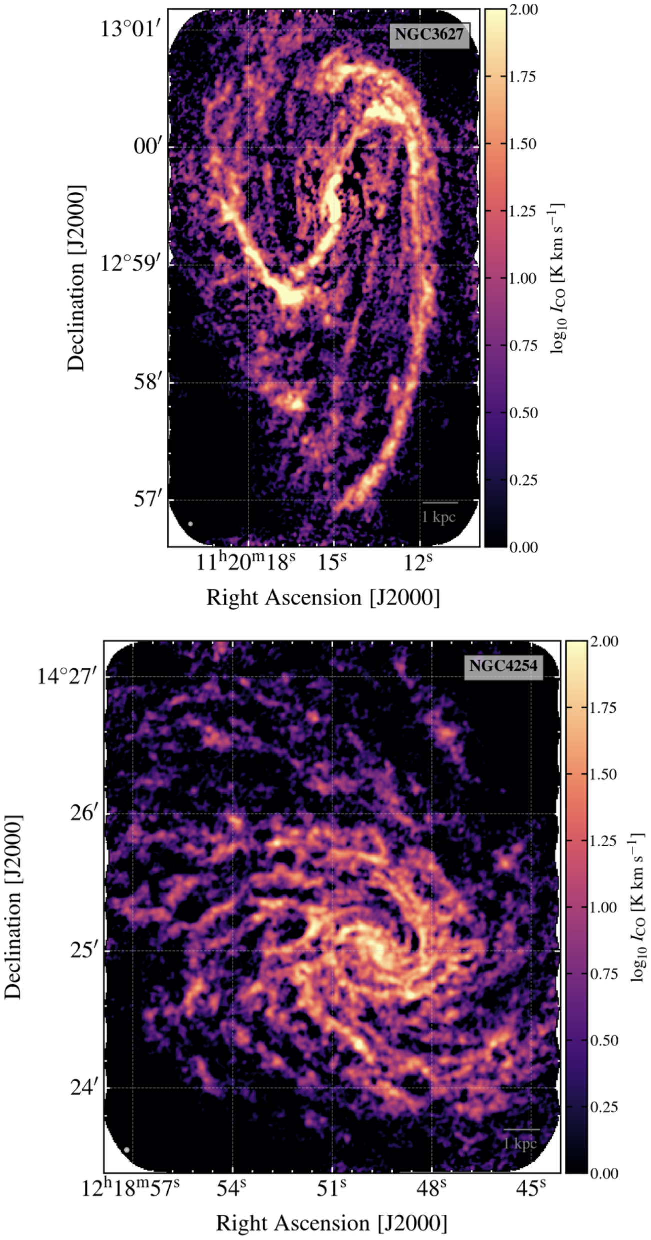

Figure 2.1 Image maps of the integrated intensity of CO (I_{CO}) measurements for PHANGS-ALMA for an example of a barred galaxy (NGC 3627) [top], and an unbarred galaxy (NGC 4254) [bottom], from the sample. Image credit: PHANGS Atlas (Leroy et al., 2021a).

2.2.1 Velocity Dispersion

The velocity dispersion of the gas is traced by the width (σ_v) of the CO emission line. There are several different ways to estimate σ_v. One common way is to calculate the second moment, or root-mean-square dispersion of the emission line profile. Another method, adopted in Leroy et al. (2021b), is to calculate what Sun et al. (2018) call an "effective width" following the method from Heyer et al. (2001). The effective width is defined by taking the integrated intensity (moment 0) and dividing by the peak brightness (Heyer et al., 2001; Sun et al., 2018, 2020). Specifically, Leroy et al. (2021a,b) use the equation:

$$\sigma_{CO} = \frac{I_{CO}}{\sqrt{2\pi}\, T_{\text{peak}}}, \tag{2.2.1}$$

where T_{peak} is the measured intensity, or brightness temperature at the line peak and has units of Kelvin (K). I_{CO} has units of K km s^{-1}, giving σ_v units of km s^{-1}. Figure 2.2 shows T_{peak} maps (on the left) and σ_v maps (on the right) from Leroy et al. (2021a,b) for the same two galaxies, barred (NGC 3627) and unbarred (NGC 4254), previously shown.

Choosing a method for estimating σ_v involves weighing benefits and costs of each. The benefit of the effective width method is that, unlike the second moment, there is less sensitivity to noise in the wings of the line profile, that is, it picks out the peak and achieves a better signal to noise ratio (Sun et al., 2018). However, the second moment method requires no assumptions about the intrinsic shape of the emission line. Both methods are influenced by the width of the channel used for the observations. A larger channel width compared to the intrinsic spectral line width will result in lower signal to noise, and can cause line broadening (Leroy et al., 2021b). To correct for this, as explained by Sun et al. (2018), the final velocity dispersion is

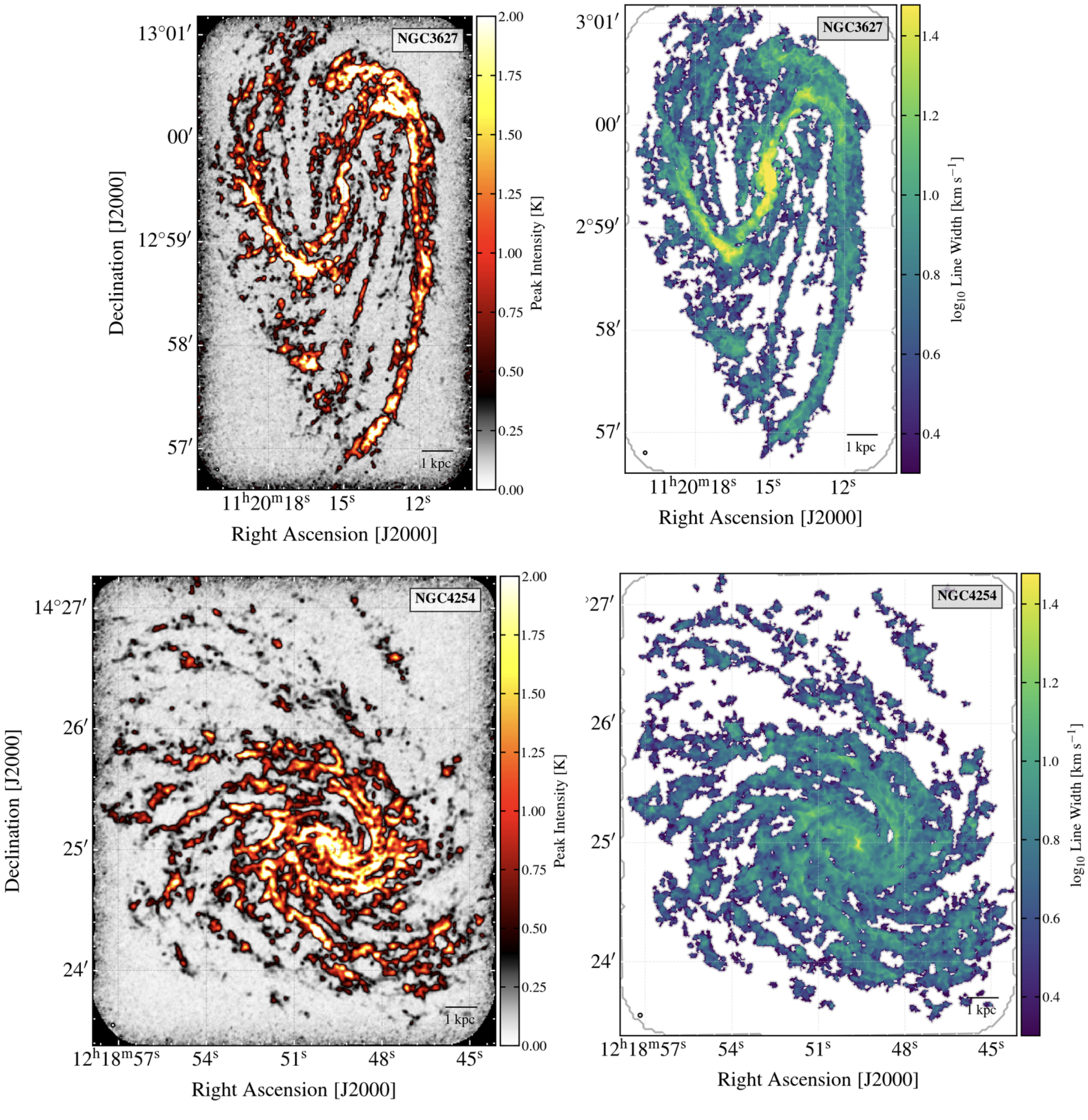

Figure 2.2 Image maps of the barred galaxy NGC 3627 [top] and unbarred galaxy NGC 4254 [bottom] showing peak brightness temperature (T_{peak}) on the left, and velocity dispersion (σ_v) on the right. T_{peak} is used to calculate σ_v from I_{CO}. Image credit: PHANGS Atlas (Leroy et al., 2021a).

given by subtracting the effective width of the spectral response curve from that of the measured line width,

$$\sigma_v = \sqrt{\sigma_{CO}^2 - \sigma_{\mathrm{response}}^2}. \tag{2.2.2}$$

Measurements of velocity dispersion near the centres of galaxies experience an effect known as “beam smearing,” which causes artificial line broadening. The effect is caused by the rotational motions of the galaxy. The velocity curve rises steeply near the centre of the galaxy which means that there will be many velocity values in a smaller area. Observations obtained with a large beam size which covers a large region (low resolution) will capture all of the velocities in that region, increasing the width of the spectral line. There is no way of disentangling all of the motions in that measurement. Until the PHANGS-ALMA survey, observations of molecular gas in nearby galaxies have had resolutions too low to be able to effectively study the velocities of the gas in galaxy centres (eg., Wilson et al. 2011). The high resolution, cloud-scale observations of PHANGS-ALMA are still affected by beam smearing, but to a much smaller degree, and therefore, can more reliably separate cloud velocities from rotational velocities. The measured line widths for the sample are in the range of $1.5 - 60$ km s^{-1}.

2.2.2 Molecular Gas Surface Density

Molecular hydrogen (H_2) is the most abundant molecule in the dense clouds of cold gas where stars form. It is difficult to observe because it has such a low mass that it requires higher temperatures to excite the rotational transitions in the molecule (Kennicutt and Evans, 2012). The carbon monoxide molecule (CO) has strong spectral lines and lives in the same star forming environment, so it can be used as a tracer for H_2. In order to estimate the H_2 from CO measurements we use a CO-to-H_2 conversion factor ($\alpha_{\rm CO}$) to convert to the physical quantities of the gas.

The molecular gas surface density (Σ_{mol}) is given by the integrated intensity of CO, the conversion factor and the appropriate line ratio (Bolatto et al., 2013):

$$\Sigma_{\rm mol} = \alpha_{\rm CO}\ R_{21}^{-1}\ I_{\rm CO}. \tag{2.2.3}$$

Here $R_{21} = 0.65$ is the CO$(2-1)$-to-CO$(1-0)$ line ratio, to relate the CO$(2-1)$ value back to the CO$(1-0)$ line described by Bolatto et al. (2013). I use the conversion factor ($\alpha_{\rm CO}$) from Sun et al. (2020), which is defined as

$$\alpha_{\rm CO} = 4.35\ Z'^{-1.6}[M_\odot\ \mathrm{pc}^{-2}(\mathrm{K\ km\ s}^{-1})^{-1}], \tag{2.2.4}$$

where $\alpha_{\rm CO}$ is metallicity-dependent and Z' is the local metallicity divided by $Z_\odot$ to put it in units of the solar metallicity. Since I_{CO} has units of K km s^{-1}, equation 2.2.3 gives $\Sigma_{\rm mol}$ in units of $M_\odot$ pc^{-2}.

In Figure 2.3 I show the increased Σ_{mol} and σ_v in the galaxy centres as was shown by Sun et al. (2020). This plot represents pixels in the image maps for these properties that are identified as being in the centre according to region masks created by Querejeta et al. (2021).

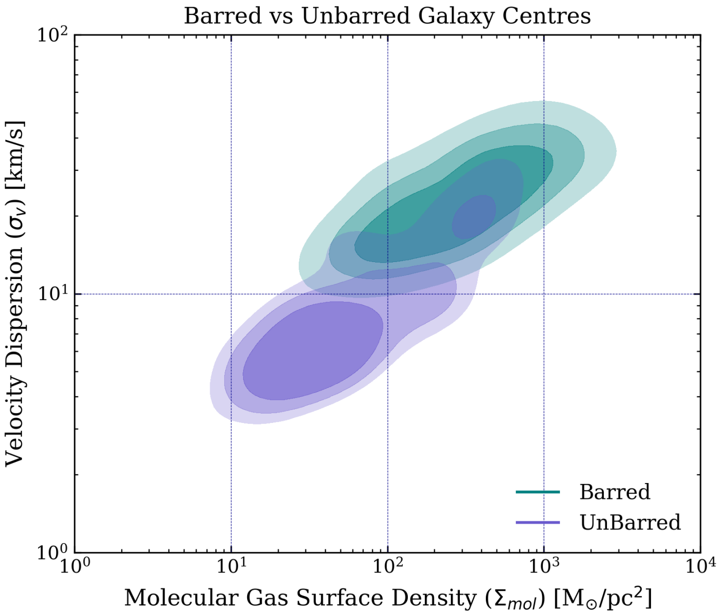

Figure 2.3 Velocity dispersion versus molecular gas surface density comparing barred and unbarred galaxy centres using the masks by Querejeta et al. (2021) for the selection. The molecular gas and velocity dispersion are both increased for the 42 barred galaxies (teal contours) versus 22 unbarred galaxies (purple contours) in the central region. The contours represent levels (0.3, 0.5, 0.7, from inner to outer contour) in the cumulative distribution function of each distribution.

2.3 Global Galaxy Properties: Barred/Unbarred

The global properties of the galaxies in my sample are listed in Sun et al. (2020) and also in Leroy et al. (2021b) where they are described in detail. I give an overview of them below and show the mean, the uncertainty on the mean, and the standard deviation in Table 2.2.

The nearby star forming galaxies in my sample have a global stellar mass range of $10^{9.27} - 10^{11.15}$ $M_\odot$. The stellar mass (M_*) of a galaxy is the most important property to measure as accurately as possible because it gives a context for how the galaxy relates to the rest of the galaxy population and it can be used to inform other galactic properties such as metallicity and SFR (Leroy et al., 2021b). For the PHANGS-ALMA sample the stellar mass is estimated using near-infrared maps from IRAC 3.6 μm (Sheth et al., 2010) and WISE1 3.4 μm (Leroy et al., 2019) in combination with locally estimated mass-to-light ratios (Leroy et al., 2021b). The adopted initial mass function is from Kroupa & Weidner (2003) (Leroy et al., 2019). The near-infrared wavelength collects light primarily from older stars and is less affected by dust extinction while light from hot young stars is captured by near- and far-ultraviolet (NUV and FUV) measurements. The mass-to-light ratios combine IR as well as NUV and FUV data from GALEX. Through a calculation detailed in Leroy et al. (2021b) the IR and mass-to-light ratios are used to derive a stellar mass surface density (Σ_*), which is then used to get M_*. The resulting stellar mass estimates from Leroy et al. (2021b) were robustly tested and compared to previous mass estimates.

The sizes of the galaxies are quantified using the derived Σ_* to get an effective radius, R_{eff} (Leroy et al., 2021b). R_{eff} is defined as the radius of the galaxy containing half of the stellar mass. This value can be affected by the presence of galactic features

Table 2.2 Global galaxy properties for 42 barred and 22 unbarred galaxies. Mean ± σ_{mean} (standard deviation) for each distribution, where $\sigma_{\text{mean}} = \sigma/\sqrt{N}$.

	log (M$_*$)	**log SFR**	**log (M$_{\text{mol}}$)**
Barred	10.3 ± 0.06 (0.42)	0.05 ± 0.07 (0.47)	9.12 ± 0.08 (0.53)
Unbarred	10.0 ± 0.09 (0.41)	-0.16 ± 0.11 (0.53)	8.92 ± 0.13 (0.59)

such as a bulge, or bright nucleus. Nevertheless, I use R_{eff} in my work defining the central region, described in section 2.4. The galaxies in the sample have a range in size of 1.1 kpc $< R_{\text{eff}} <$11.8 kpc.

The star formation rate (SFR) is estimated in the same way for both the global and resolved data, using the prescription from Leroy et al. (2019). The method uses GALEX FUV and NUV maps combined with IR maps from WISE3 (12 μm) and WISE4 (22 μm). Similar to the process for deriving the stellar mass of galaxies, the SFR is derived by combining the UV and IR measurements in order to get an estimated count of the population of stars, including both exposed and obscured young stars. Young stars obscured by dust, can be observed using near-IR measurements (Leroy et al., 2019). A linear combination of UV and IR maps, along with a scaling relation for the luminosity in each band, is used to measure the star formation rate (Leroy et al., 2019; Querejeta et al., 2021). The SFR range for the sample is $0.06 - 14.34\ M_\odot\ \text{yr}^{-1}$. In Figure 2.4 the centre plot shows SFR as a function of M_* in log space and compares barred versus unbarred galaxies.

In order to calculate the global molecular gas mass (M_{mol}) for the galaxies in my sample I used the global CO luminosity (L_{CO}) from Leroy et al. (2021b), listed in their Table 4. They estimate L_{CO} by integrating over a lower resolution ALMA CO$(2-1)$ data cube with 17 arcsec resolution. Leroy et al. (2021b) explain that the

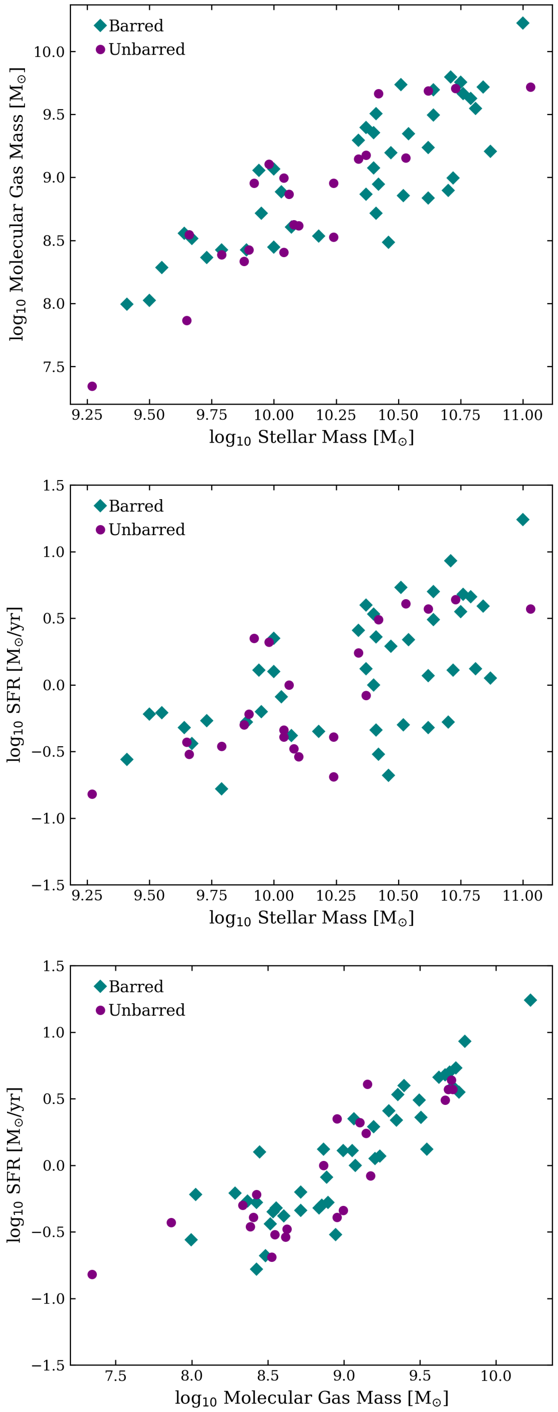

Figure 2.4 Barred versus unbarred global galaxy properties. [Top] $M_{\rm mol}$ as a function of M_*; [Middle] SFR as a function of M_*; [Bottom] SFR as a function of $M_{\rm mol}$.

lower resolution allows the signal to be identified easily over the whole galaxy. Similar to equation 2.2.3, the conversion factor (α_{CO}) and the appropriate line ratio are used to calculate M_{mol}, this time multiplied by the integrated luminosity:

$$M_{\mathrm{mol}} = \alpha_{\mathrm{CO}}\ R_{21}^{-1}\ L_{\mathrm{CO}}, \tag{2.3.1}$$

where α_{CO} is as in equation 2.2.4, $R_{21} = 0.65$ is again the CO$(2-1)$-to-CO$(1-0)$ line ratio, and L_{CO} is the integrated luminosity. In this case, since L_{CO} has units of K km s^{-1} pc^2, M_{mol} has units of $M_{\odot}$.

The top and bottom scatter plots in Figure 2.4 compare M_{mol} with two other key properties, for barred (teal) versus unbarred (violet) galaxies. In the top plot M_{mol} is shown as a function of M_*, and in the bottom plot SFR is shown as a function of M_{mol}, a version of the Kennicutt-Schmidt relation.

It is common in the literature to compare various galactic properties by looking at their ratios. The gas mass fraction (f_{mol}) normalizes the molecular gas mass by the stellar mass which shows how much molecular gas there is compared to stars. The specific star formation rate (sSFR) is given by SFR divided by the stellar mass, which measures how many stars form per unit mass of stars. The depletion time (t_{dep}) is the molecular gas mass normalized by SFR which tells us how long it takes for all the gas to be used up to form stars, assuming a constant SFR. These three ratios are given respectively as follows:

$$f_{\mathrm{mol}} = \frac{M_{\mathrm{mol}}}{M_*}, \qquad \mathrm{sSFR} = \frac{\mathrm{SFR}}{\mathrm{M}_*}, \qquad \mathrm{t}_{\mathrm{dep}} = \frac{\mathrm{M}_{\mathrm{mol}}}{\mathrm{SFR}}. \tag{2.3.2}$$

The box plots in Figure 2.5 graphically represent the distributions of each ratio

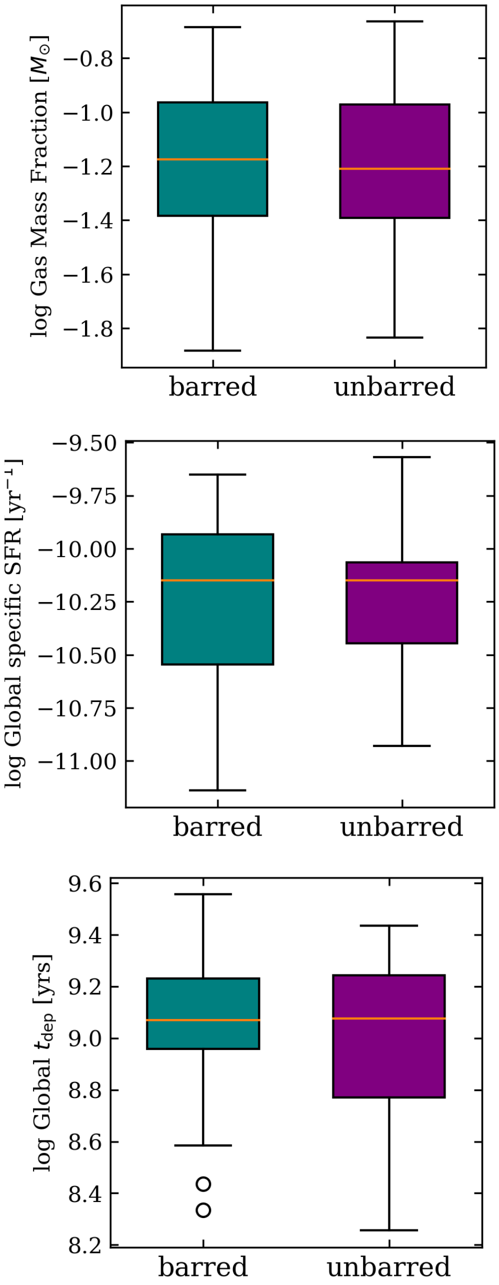

Figure 2.5 Boxplots showing the distributions of global property ratios, from top to bottom, molecular gas mass fraction, specific star formation rate, and molecular gas depletion time. Each property is separated into barred and unbarred galaxies.

from top to bottom, f_{mol}, sSFR and t_{dep}, for barred (teal) and unbarred (purple) galaxies. For each box plot, the median is shown as an orange line, the box represents the interquartile range (IQR) between the first and third quartiles of the distribution and the whiskers extend out to 1.5 IQR on either side. Outliers are shown by the circles and are either $>$ 1.5 IQR (above the top whisker) or $<$ 1.5 IQR (below the bottom whisker). The boxplots suggest that there is no difference between the barred and unbarred samples for the global property ratios.

2.4 Choosing Galactic Central Regions

Finding a consistent definition for the size of the galactic central region to use in the analysis was an important first step in my research. This is a challenging question given the differing distances to, and sizes of, the galaxies in the sample, as well as the variety in the galaxy morphological features. The sample contains only nearby star forming spiral galaxies, but the structure in the central region can vary dramatically depending on features such as the size of the galactic bulge, whether there is a galactic bar, the strength and size of a galactic bar, or whether there is an AGN in the centre. For example, if the bar is short, it may lie completely inside the central region. In contrast, for a very large bar with a central star forming ring, that ring may dominate the central region.

As part of the PHANGS collaboration, Querejeta et al. (2021) developed a series of masks as a way to select different features of a galaxy. The mask regions include centres, stellar bars, spiral arms, interarm regions, and outer disk regions. Sun et al. (2020) define centres using these masks. The masks are robust and designed to accommodate different types of stellar structures that could be responsible for an excess brightness at the centre of a galaxy, such as an unresolved nuclear bar or ring. Querejeta et al. (2021) use Spitzer 3.6 μm images to define the mask regions. In some cases, they identify asymmetrical structures in the centres through visual inspection and adjust the masks accordingly. However, there are a few reasons to consider alternative approaches for choosing the central regions.

Due to the method of selecting which pixels are assigned to the centre masks, it is possible that not every galaxy has pixels defined for each region, so galaxies may not all have a "centre" mask (Querejeta et al., 2021). The Querejeta centre masks may be dependent on distance, for example a compact central structure is more easily identified in a nearby galaxy than a more distant one. As an alternative I explored a more physically based definition of the galactic centre; this approach would also make it easier to extend my sample by including other surveys in future. One option is to define the centre as the central 1 kpc of the galaxy. This method has the advantage that it is not dependent on distance to the galaxy, but it does not take into account differences in the size of different galaxies. A distance of 1 kpc from the centre would represent a larger percentage of a smaller galaxy compared to a more massive one. As a comparison, I also considered the centre as a percentage of the effective radius of the galaxy. I considered several different percentages out to a maximum of 25% of $R_{\rm eff}$. I compared these percentages of radius to the results from the 1 kpc definition as well as the centre masks from Querejeta et al. (2021) and find that $10\%R_{\rm eff}$ is similar to the centre masks while $25\%R_{\rm eff}$ is closer to the 1 kpc radius.

2.5 Resolved Central Regions: Barred/Unbarred

2.5.1 Hexagonal Pixels

The native spatial resolution for the PHANGS-ALMA Large Program data reaches down to high resolutions where each pixel represents cloud scales (150pc). We have the measurements of the molecular gas surface density as well as velocity dispersion at these scales. However, one of the key physical properties that we want to analyse is SFR, and there is currently no way to calculate SFR for the resolved high resolution pixels. To solve this problem the PHANGS collaboration developed 1.5 kpc hexagonal "pixels" which combine the resolved data together. These hexagons do not overlap and so each hexagon represents a unique area of the galaxy. Their size is measured to be 1.5 kpc between the centres of two pixels side-by-side. SFRs have been calculated by Leroy et al. (2021b) for each of these pixels using the same prescription described for global properties in section 2.3, GALEX NUV, WISE 12μm following Leroy et al. (2019). My definition of the centre of a galaxy extends out to the size of one pixel, so I have one hexagonal central pixel per galaxy. Figure 2.6 shows image maps of NGC 4254 as an example to show the hexagonal pixel in the centre and give a sense of the size of the central region.

As a result of the fact that we now have one pixel which combines all of the high resolution measurements of $\Sigma_{\rm mol}$ and σ_v, it is necessary to calculate an average value to use for the analysis. The PHANGS team has calculated this for $\Sigma_{\rm mol}$ in two ways and I explore both of them in my linear regression analysis.

The first way is to take the average of all the pixels in the hexagon. We call this method the region-average (RA) $\Sigma_{\rm mol}$. This has the effect of smoothing out all the

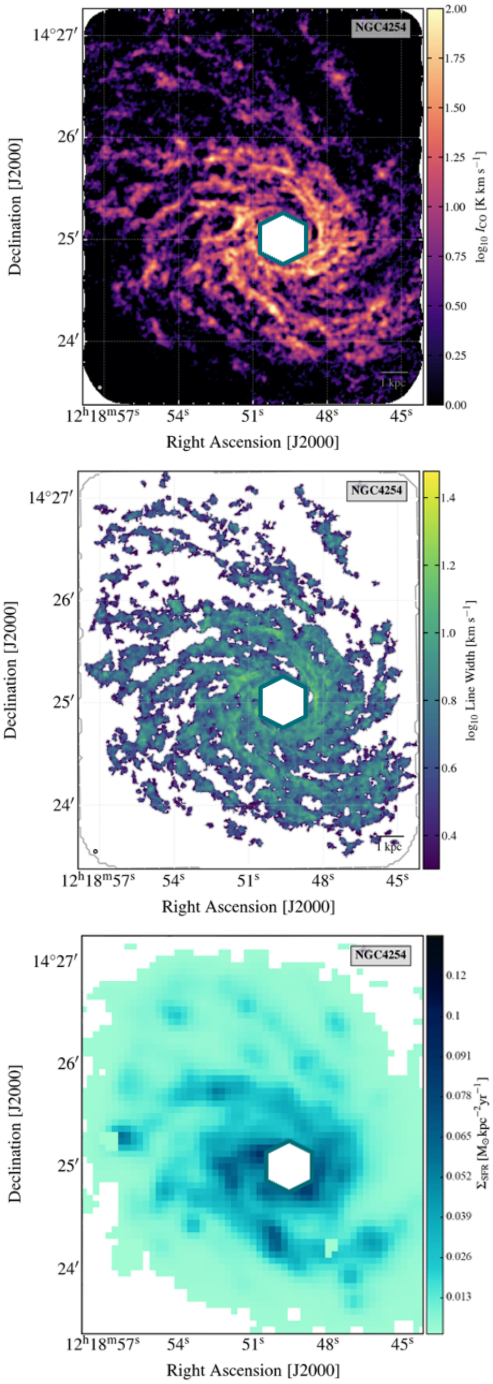

Figure 2.6 Image maps of NGC 4254 showing I_{CO} [top] and σ_v [middle] from PHANGS-ALMA (Leroy et al., 2021a), and SFR [bottom] from GALEX, WISE measurements (Jiménez-Donaire et al., 2023), with the 1.5 kpc hexagonal pixel displayed over the centre.

pixels over the whole hexagonal region and mimics what a low resolution Σ_{mol} map would measure. The second way is to take a flux-weighted (FW) mean value so that some of the information about how the density changes over the hexagonal region is maintained (Leroy et al., 2013a). The velocity dispersion is a flux-weighted mean calculation, but this has only been calculated in one way.

2.5.2 Properties of the Central Regions

The three key properties (one averaged in two ways) that I have used in my analysis are region-average Σ_{mol}, flux-weighted mean Σ_{mol}, flux-weighted mean σ_v, and Σ_{SFR} for the central hexagonal pixel. Figure 2.7 shows each of the four properties in a boxplot comparing the barred and unbarred galaxy distributions. As was done previously, the boxplots each show the median of the distribution as an orange line, the box encloses the region between the first and third quartiles, and the vertical lines extend out to the non-outlier extremes of the distributions. Outliers are shown as black circles. Mean, uncertainty on the mean and standard deviation for each distribution are listed in Table 2.3.

Table 2.3 Resolved gas properties in the central region of all galaxies in the sample, then separated into 42 barred and 22 unbarred galaxies. Mean ± σ_{mean} (standard deviation) for each distribution, where $\sigma_{\mathrm{mean}} = \sigma/\sqrt{N}$.

	$\log \Sigma_{\mathrm{mol,RA}}$ [$\mathrm{M_\odot\ pc^{-2}}$]	$\log \Sigma_{\mathrm{mol,FW}}$ [$\mathrm{M_\odot\ pc^{-2}}$]	σ_{v} [$\mathrm{km\ s^{-1}}$]	$\log \Sigma_{\mathrm{SFR}}$ [$\mathrm{M_\odot\ kpc^{-2}\ yr^{-1}}$]
All	1.68±0.08(0.61)	2.00±0.09(0.68)	1.05±0.04(0.33)	-1.40±0.08(0.64)
Barred	1.83±0.09(0.59)	2.21±0.11(0.62)	1.17±0.05(0.30)	-1.24±0.10(0.61)
Unbarred	1.39±0.13(0.56)	1.60±0.15(0.61)	0.84±0.07(0.27)	-1.70±0.14(0.59)

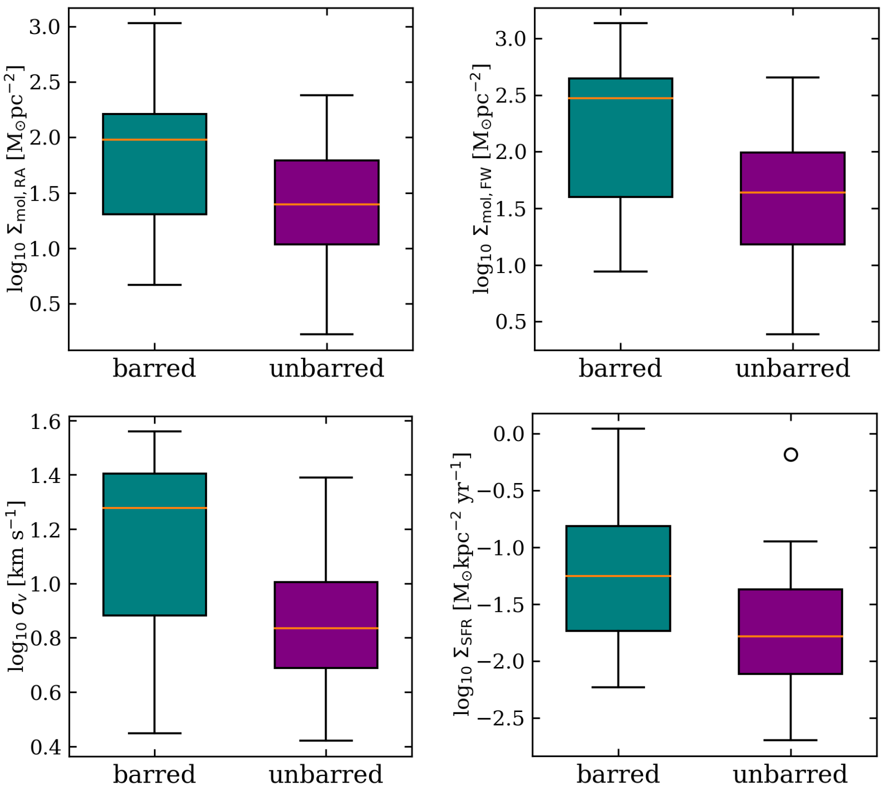

Figure 2.7 Boxplots showing the distributions of each individual sample. Each property is separated into barred (42) and unbarred (22) galaxies.

The box plot of the flux-weighted $\Sigma_{\rm mol}$ has a significantly higher median value for the barred galaxies than the region-average $\Sigma_{\rm mol}$, as shown by the Anderson-Darling test results discussed in Chapter 3. The flux-weighted σ_v is similarly varied between barred and unbarred galaxies. The unbarred $\Sigma_{\rm SFR}$ has an outlier which lies far from the rest of the galaxies in that sample. The outlier is the galaxy Circinus which has a strong AGN so this high apparent rate of star formation is likely spurious. It is worth noting that the sample size is pretty small with only 22 unbarred galaxies.

2.6 Statistical Methods

2.6.1 Anderson-Darling Test

The Anderson-Darling test (AD-test) is a goodness of fit statistic (Scholz and Stephens, 1987), similar to the Kolmogorov-Smirnov test (KS-test). The statistic measures how well a distribution of data fits a specific distribution such as a normal distribution. In the case of the k-sample AD-test two independent distributions can be compared to each other to determine if they are drawn from the same population. This is the test I conducted for several properties from the sample. The AD-test was chosen instead of the KS-test because AD-tests are well suited for small samples sizes of less than 50 members (Scholz and Stephens, 1987). The null hypothesis for the AD-test is that the samples are drawn from the same distribution. We accept the null hypothesis for p-values > 0.05. For p-values close to 0.05 we have weak evidence against the null hypothesis, and any p-values < 0.01 we have moderate to strong evidence against the null hypothesis, suggesting that the distributions are not drawn from the same population.

Running statistical tests in python is commonly done using scipy and is usually successful. However, the AD-test in scipy does not give robust results. I used R and had much better results. I used the package kSamples in R Studio to run the AD-test for multiple distributions, in my case $k = 2$ for two distributions. This AD-test in R returns the AD criterion for k samples as well as the AD test statistic (T). I show my results in Chapter 3.

2.6.2 Linear Regression: Linmix

Linear regression is a useful statistical tool when working with scatter plots of distributions that might be related. The comparison of gas properties such as molecular gas surface density ($\Sigma_{\rm mol}$), velocity dispersion (σ_v), and star formation rate surface density ($\Sigma_{\rm SFR}$) can help us understand how these quantities vary between barred and unbarred galaxies in these environments. These properties are expected to be related in different ways so a linear regression analysis on various 2-D scatter plots will tell us how these relations for the centres of galaxies compare to previous similar analyses.

Linmix is a hierarchical Bayesian python software package for line fitting. It generates the most probable best fit line for the input data. The underlying code generates an MCMC routine which finds the best fit slope and intercept for two distributions x and y with uncertainties on each. Using it is straight forward, we download and import the code, and then write a function to run it.

The inputs for linmix are the distribution and uncertainty for the x-axis, the distribution and uncertainty for the y-axis, and as output it generates a 95% confidence interval for the best fit slope and intercept values, a best fit slope with uncertainty and a best fit intercept with uncertainty.

One of the steps taken to prepare the distributions for analysis was to mask some non-detections in the data that showed up as 'nan'. As a result, we needed to make sure any galaxy that was removed for this reason from one sample, was also removed from any sample to which this was being compared.

Chapter 3

Statistical Analysis and Results

My research project was originally motivated after seeing the results of Sun et al. (2020) and Querejeta et al. (2021) from the PHANGS collaboration who showed differences in the molecular gas at the centres of barred versus unbarred galaxies in the nearby universe, using cloud scale observations. Specifically, Sun et al. (2020) found higher molecular gas surface density and velocity dispersion in barred galaxy centres. The high resolution achieved by PHANGS-ALMA makes it possible to study these properties in galaxy centres with less worry about the effects of beam smearing for the velocity dispersion measurements. Higher velocity dispersion can be an indicator of physical properties such as turbulence in the gas. It was clear from these results that a study of the centres of these galaxies in more detail was worthwhile.

I have analysed three properties of the gas and star formation that play an important role in the physics in that region; region-average Σ_{mol}, flux-weighted mean Σ_{mol}, flux-weighted mean σ_v, and Σ_{SFR} for the central hexagonal pixel. I have done a statistical analysis to understand how these quantities vary in the central region between barred and unbarred galaxies. I have further explored how the results change if we adjust the sample in two ways, first, by removing galaxies with a known active galactic nucleus (AGN), and second, by considering the environment where the galaxy lives (whether in a cluster or in the field). In this chapter I show and discuss the results of my analysis in the context of our current understanding of galaxy centres and in particular barred galaxies.

3.1 Anderson-Darling Test Results

I start by considering each of the three properties individually and comparing the barred galaxy distribution with the unbarred galaxy distribution. I run the Anderson-Darling test (AD-test) for goodness of fit to see if the shape of the barred versus unbarred distributions is the same, or in other words, to see if they are drawn from the same population. The AD-test was developed in a way that makes it useful for small samples sizes of less than 50 members. It begins to breakdown when the sample size gets too low, less than 5 members. When I consider my whole sample, they divide into 42 barred and 22 unbarred galaxies.

Recall that for the AD-test, the null hypothesis states that the samples are drawn from the same distribution, so evidence against the null hypothesis suggests that the distributions are not drawn from the same population. I use Table 3.1 to evaluate the result of each test.

Table 3.1 AD-test Evaluation

p-value	**code**	**test result**
> 0.1	$+$	accept null hypothesis
$[0.05, 0.1]$	$\circ$	weak evidence against the null hypothesis
< 0.05	$\bullet$	moderate to strong evidence against the null hypothesis

Table 3.2 Statistical results of Anderson-Darling test for goodness-of-fit comparing 42 barred and 22 unbarred galaxies for each property. In each case the AD statistic, the p-value, and the evaluation are listed.

Property	**AD statistic**	**p-value**	**evaluation**
$\Sigma_{\mathrm{mol,RA}}$	3.6	0.0115	●
$\Sigma_{\mathrm{mol,FW}}$	6.8	0.00078	●
σ_{v}	8.3	0.00023	●
Σ_{SFR}	3.5	0.013	●
t_{dep}	0.034	0.34	+

Table 3.2 shows the results of the AD-test comparing barred and unbarred galaxies. All of the properties, $\Sigma_{\mathrm{mol,RA}}$, $\Sigma_{\mathrm{mol,FW}}$, σ_v, and Σ_{SFR}, show strong evidence against the null hypothesis suggesting that they are not from the same population. The properties that show the strongest evidence of this are the two that are flux weighted over the hexagonal pixel. This is noteworthy because the flux weighted mean over the pixel takes the underlying high resolution measurements into account, so the resolution of the data makes a difference in the statistics.

The depletion time t_{dep} is the ratio of the molecular gas surface density to the SFR surface density and represents how long it takes to use up all the gas in the galaxy to form stars. Here, we see that the two distributions of barred and unbarred galaxies are drawn from the same population. So even though the two properties that make up the depletion time are from different populations, their ratio is not. The similar depletion times suggest that the SFR surface density varies roughly linearly with the molecular gas surface density in both barred and unbarred galaxy centres.

3.2 Linear Regression Results

The second part of my statistical analysis considers the properties in a two-dimensional context by performing a linear regression analysis on five different comparisons of the four distributions. The five comparisons are as follows:

1. Region-average $\Sigma_{\rm mol}$ vs σ_v
2. Flux-weighted mean $\Sigma_{\rm mol}$ vs σ_v
3. Region-average $\Sigma_{\rm mol}$ vs σ_v (smaller range)
4. Region-average $\Sigma_{\rm mol}$ vs $\Sigma_{\rm SFR}$
5. $\Sigma_{\rm SFR}$ vs σ_v

Items 1, 2, and 3 compare the same pair of gas properties in different ways. The comparison between the molecular gas surface density and velocity dispersion is important because it was in this distribution that we saw the higher values for barred galaxies in Sun et al. (2020), so we want to analyse that variation. Items 1 and 2 look at the two different ways of calculating $\Sigma_{\rm mol}$ discussed previously, and scatter plots of these distributions are shown in Figure 3.1. Item 3 considers what happens when we remove the barred galaxies with the highest values and the unbarred galaxies with the lowest values so that the distributions match more closely in dynamic range. It is easiest to see the reason for this consideration when looking at the plots in Figure 3.2: we can see that the offset between barred and unbarred galaxies seen in the top panel remains nearly unchanged when we truncate the range of data points.

Item 4 is the Kennicutt-Schmidt (KS) relation ($\Sigma_{\rm mol}$ vs $\Sigma_{\rm SFR}$) shown in Figure 3.3. It does not make sense to compare $\Sigma_{\rm SFR}$ with the flux weighted mean $\Sigma_{\rm mol}$

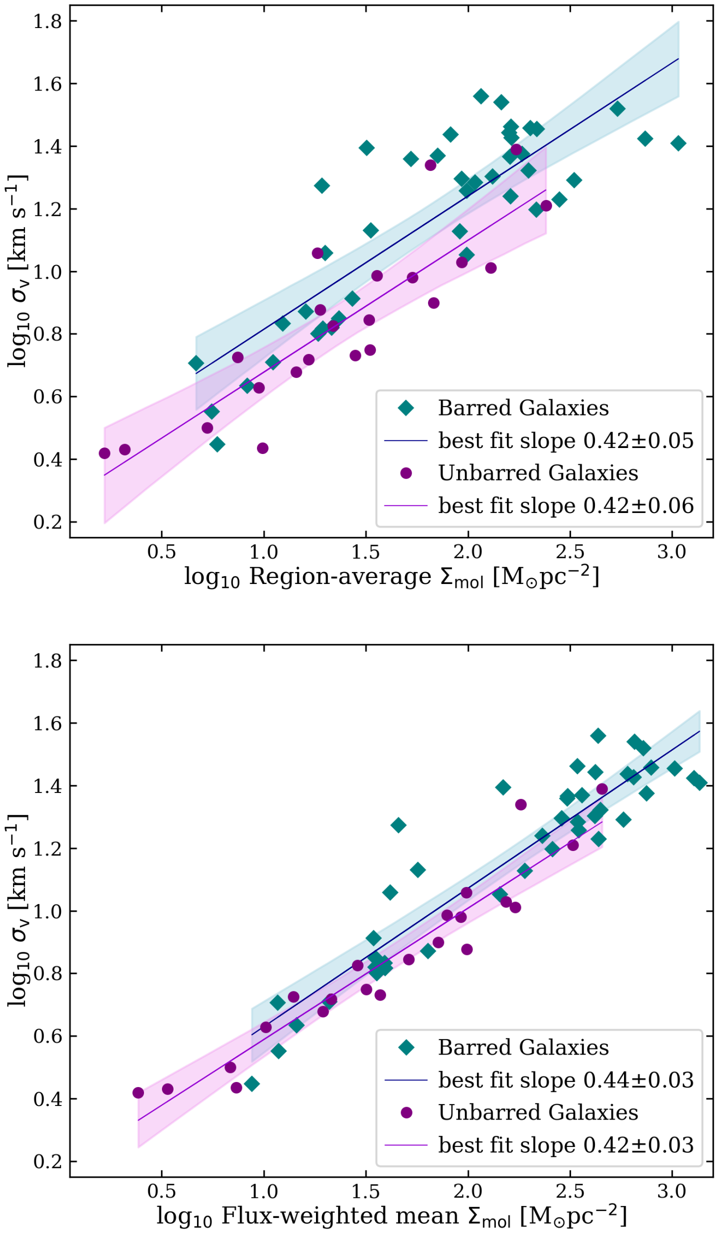

Figure 3.1 Barred versus unbarred resolved galaxy properties, [Top] σ_v as a function of $\Sigma_{\mathrm{mol,RA}}$; [Bottom] σ_v as a function of $\Sigma_{\mathrm{mol,FW}}$. Best fit lines generated with Linmix with slope and intercept uncertainties shown in shaded regions. These two scatter plots show how the distributions change based on how Σ_{mol} is averaged over the hexagon pixel. There is less scatter when comparing the two flux weighted distributions in the bottom plot.

Table 3.3 Statistical results of Linmix linear regression comparing 42 barred and 22 unbarred galaxies for each comparison. In each case the resulting Linmix best fit slopes (with uncertainty) and intercepts (with uncertainty) are listed.

	Slope		
	All	**Barred**	**Unbarred**
$\Sigma_{\mathrm{mol,RA}}$ vs σ_v	0.46 ± 0.04	0.42 ± 0.05	0.42 ± 0.06
$\Sigma_{\mathrm{mol,RA}}$ vs σ_v (small range)	0.50 ± 0.04	0.48 ± 0.05	0.45 ± 0.08
$\Sigma_{\mathrm{mol,FW}}$ vs σ_v	0.45 ± 0.02	0.44 ± 0.03	0.42 ± 0.03
$\Sigma_{\mathrm{mol,RA}}$ vs Σ_{SFR}	0.93 ± 0.06	0.90 ± 0.09	0.94 ± 0.12
Σ_{SFR} vs σ_v	0.42 ± 0.04	0.37 ± 0.05	0.40 ± 0.05
	Intercept		
	All	**Barred**	**Unbarred**
$\Sigma_{\mathrm{mol,RA}}$ vs σ_v	0.28 ± 0.06	0.39 ± 0.09	0.26 ± 0.09
$\Sigma_{\mathrm{mol,RA}}$ vs σ_v (small range)	0.22 ± 0.08	0.31 ± 0.09	0.20 ± 0.13
$\Sigma_{\mathrm{mol,FW}}$ vs σ_v	0.15 ± 0.04	0.19 ± 0.07	0.17 ± 0.06
$\Sigma_{\mathrm{mol,RA}}$ vs Σ_{SFR}	-2.95 ± 0.11	-2.89 ± 0.16	-3.01 ± 0.18
Σ_{SFR} vs σ_v	1.64 ± 0.06	1.63 ± 0.07	1.52 ± 0.10

because Σ_{SFR} is averaged over the whole hexagonal pixel, so it should be compared with the smooth region average for the Σ_{mol}. This was the reason for using the larger hexagonal pixels. Item 5 is a distribution that is not as often seen in the literature Σ_{SFR} vs σ_v, but could reveal some connection between turbulence and SFR, so is worth exploring. This relation is shown in Figure 3.4.

Figures 3.1, 3.2, 3.3, and 3.4 show my results of the best fit lines, where the shaded regions are the slope and intercept uncertainties. These uncertainties are calculated as the 95% confidence intervals for the slopes and intercepts. The uncertainties for the hexagonal pixel in the centre of each galaxy are quite small so error bars do

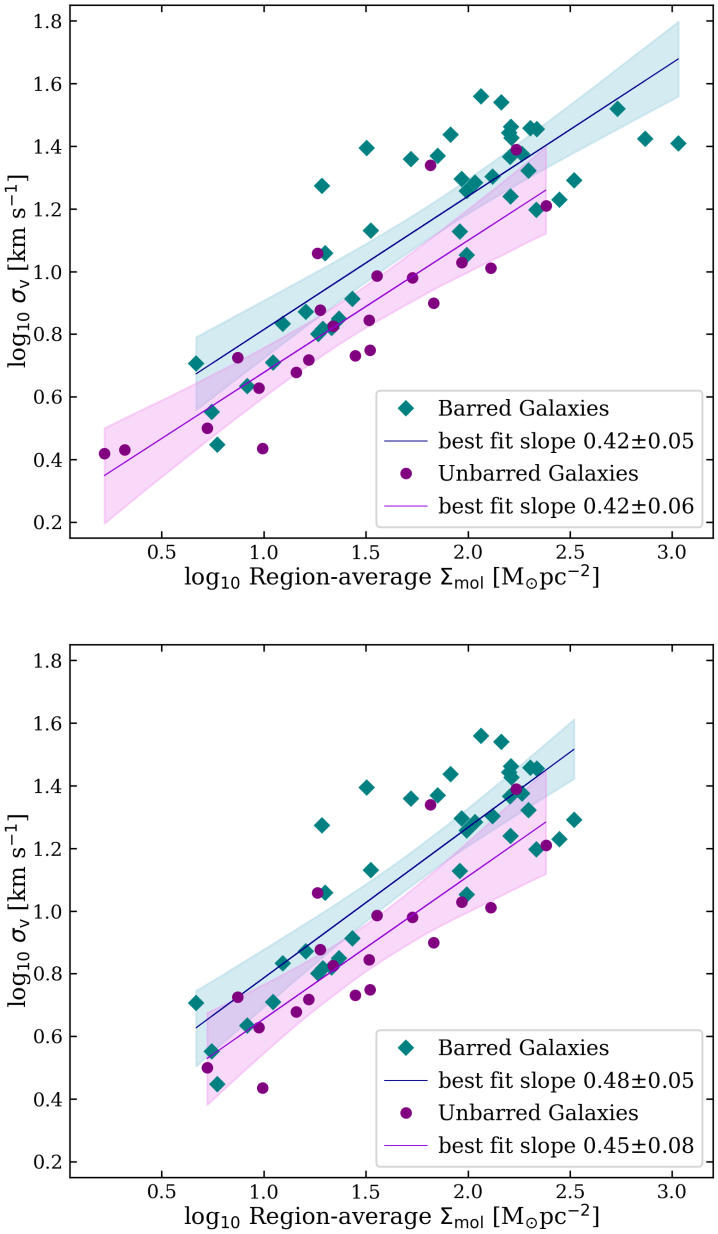

Figure 3.2 Barred versus unbarred resolved galaxy properties. [Top] σ_v as a function of $\Sigma_{\mathrm{mol,RA}}$ (from Fig. 3.1); [Bottom] σ_v as a function of $\Sigma_{\mathrm{mol,RA}}$ with a smaller range. Best fit lines generated with Linmix with slope and intercept uncertainties shown in shaded regions. The offset between barred and unbarred galaxies is not affected by truncating the dataset.

not show up for each point on these plots, which is expected because these data represent the centres of the galaxies where the intensity is the highest. Since there is high signal to noise in the centres in comparison to the rest of the galaxy, the measurement uncertainties tend to be smaller in the centres. The numerical linear regression results are listed in Table 3.3.

The different ways of calculating the $\Sigma_{\rm mol}$, shown in Figure 3.1, have a noticeable impact on the offset between barred and unbarred galaxies in these plots. The offset is much greater for the region-average $\Sigma_{\rm mol}$ than for the flux-weighted mean $\Sigma_{\rm mol}$. Both of these comparisons show the higher $\Sigma_{\rm mol}$ and $\sigma_{\rm v}$ for barred galaxy centres, which support the expectation that there is extra turbulence in bars due to inflow of gas along the bar.

The Linmix results also show differences in the uncertainty range on the slope and intercept depending on the distribution. Similar plots use the same scale in order to make comparisons clear. When the data extend over the whole range of the x- and y-axes we expect a narrower uncertainty on the best fit line, which we see here (eg. bottom panel of Figure 3.1). We see a wider uncertainty range when the distribution is smaller, as is especially noticeable in the 'smaller range' plot (bottom in Figure 3.2) where the galaxies with the highest and lowest values in region-average $\Sigma_{\rm mol}$ are removed. However, comparing the two panels of Figure 3.2 the offset between the barred and unbarred lines is not very different. The only visible difference seems to be the width of the spread, which is wider due to the narrower range of data on the x-axis.

Figure 3.3 shows the Kennicutt-Schmidt relation $\Sigma_{\rm SFR}$ vs $\Sigma_{\rm mol}$. The expected value for this relation is a slope of around 1.0 (eg., Jiménez-Donaire et al. 2023).

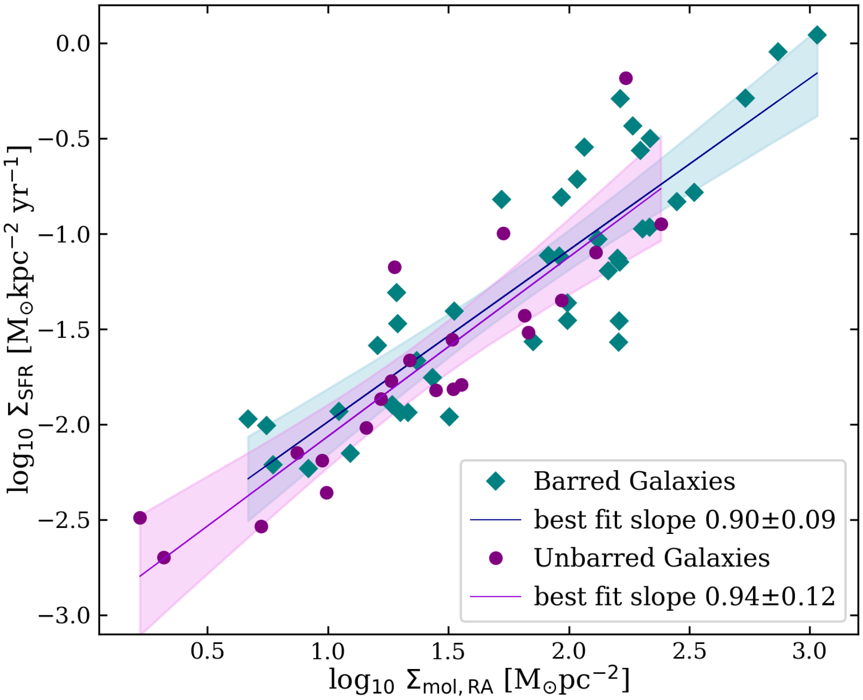

Figure 3.3 The Kennicutt-Schmidt relation $\Sigma_{\rm SFR}$ as a function of $\Sigma_{\rm mol,RA}$ for barred versus unbarred resolved molecular gas observations. Best fit lines generated with Linmix with slope and intercept uncertainties shown in shaded regions.

The slope I find for $\Sigma_{\rm mol,RA}$ is 0.90 ± 0.09 with intercept -2.89 ± 0.16 for barred and 0.94 ± 0.12 with intercept -3.01 ± 0.18 for unbarred and very little offset between the two distributions. I have compared these values to recent work using resolved data, such as Jiménez-Donaire et al. (2023) who study the VERTICO sample of galaxies in the Virgo cluster. They find a slope of 0.91±0.08 and intercept of -3.15±0.11 for the data at 1.2 kpc resolution, which is comparable to my 1.5 kpc pixels. Jiménez-Donaire et al. (2023) also include a compilation of KS relations from the literature. My result suggests that the resolved KS relation is the same for centres as for the whole galaxy.

Figure 3.4 shows $\sigma_{\rm v}$ as a function of $\Sigma_{\rm SFR}$ which is not as commonly found in the literature, as far as we've seen, especially for galaxy centres. Due to the difference in offset of the two distributions we see that σ_v increases for the barred galaxy centres which is worth exploring further. Higher velocity dispersion can indicate more turbulence in the gas which can impact star formation.

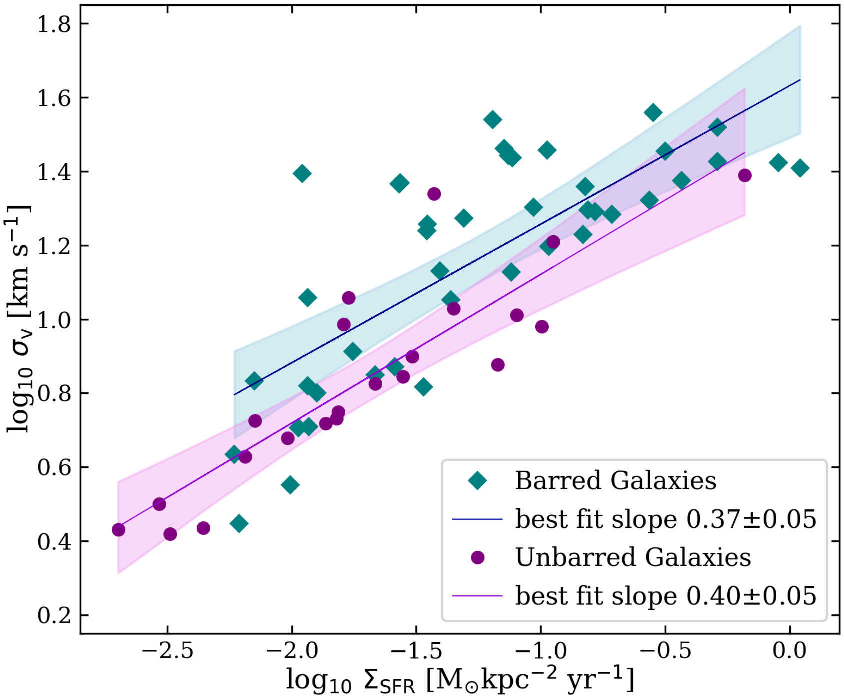

Figure 3.4 σ_v as a function of $\Sigma_{\rm SFR}$ for barred versus unbarred resolved galaxy properties. Best fit lines generated with Linmix with slope and intercept uncertainties shown in shaded regions. Barred galaxies also show increased σ_v in the central region.

3.3 Active Galactic Nucleus

The presence of an active galactic nucleus (AGN) in the centre of a galaxy is expected to greatly enhance the properties that I am studying. Increased CO intensity and molecular gas surface density could be from an AGN (Bolatto et al., 2021; Liu et al., 2023). Studies using hydrodynamical simulations as well as observations show that galactic outflows caused by AGN can reach high speeds, ≥ 1000 km s^{-1}, coming out from the centre of the galaxy to spatial scales in the range of $1 - 10$ kpc (Costa et al., 2014). This would increase the measured velocity dispersion in the CO observations. Shock-driven compression of the gas caused by outflows can induce star formation (Stuber et al., 2021) which would cause the increases we see as well. In order to see if the AGN are the main cause of the increased properties in the data, I did the same statistical analysis with a new sub-sample with all of the galaxies with AGN removed. AGN are identified using optical spectroscopy (Véron-Cetty and Véron, 2010), and I use the classification of which galaxies have an AGN from Stuber et al. (2021), and list these in my Table 2.1.

I have again compared the gas properties of barred and unbarred galaxies to study the impact of the presence of an AGN. I divided the original sample up as follows with sample size shown in brackets:

1. Barred galaxies with AGN (12)
2. Unbarred galaxies with AGN (3)
3. Barred galaxies without AGN (30)
4. Unbarred galaxies without AGN (19)

I looked at various comparisons and noted that the sample of unbarred galaxies with AGN is too small for any useful statistics. I settled on two combinations to study, barred and unbarred galaxies without AGN, and barred galaxies with and without AGN. I then did the same statistical tests (AD-test and linear regression using Linmix) as was done for the full sample.

3.3.1 Anderson-Darling Test Results Excluding AGN

Table 3.4 Statistical results of Anderson-Darling test for goodness-of-fit for the sample that considers the presence of an AGN. In each case the AD statistic, the p-value, and the evaluation are listed.

	Property	**AD statistic**	**p-value**	**evaluation**
Barred (30) vs Unbarred (19) (with no AGN)	$\log \Sigma_{\mathrm{mol,RA}}$	1.3	0.09	○
	$\log \Sigma_{\mathrm{mol,FW}}$	4.0	0.0087	●
	σ_{v}	5.4	0.0025	●
	Σ_{SFR}	1.8	0.058	○
	t_{dep}	-0.146	0.421	+
AGN (12) vs no AGN (30) (Barred galaxies)	$\log \Sigma_{\mathrm{mol,RA}}$	4.7	0.0048	●
	$\log \Sigma_{\mathrm{mol,FW}}$	8.4	0.00022	●
	σ_{v}	10.2	4.6×10^{-5}	●
	Σ_{SFR}	5.2	0.0031	●
	t_{dep}	-0.153	0.424	+

Table 3.4 shows the results of the AD-test for goodness-of-fit for the sample of barred versus unbarred galaxies with no AGN and for the barred galaxies with and without AGN. When we take away AGN from the barred and unbarred galaxies, they are still shown to be from different populations. The region average Σ_{mol} is more unclear with a p-value of 0.09, but the flux-weighted mean Σ_{mol} which resolves the cloud scales suggests more strongly with a p-value of 0.0087 that they are different

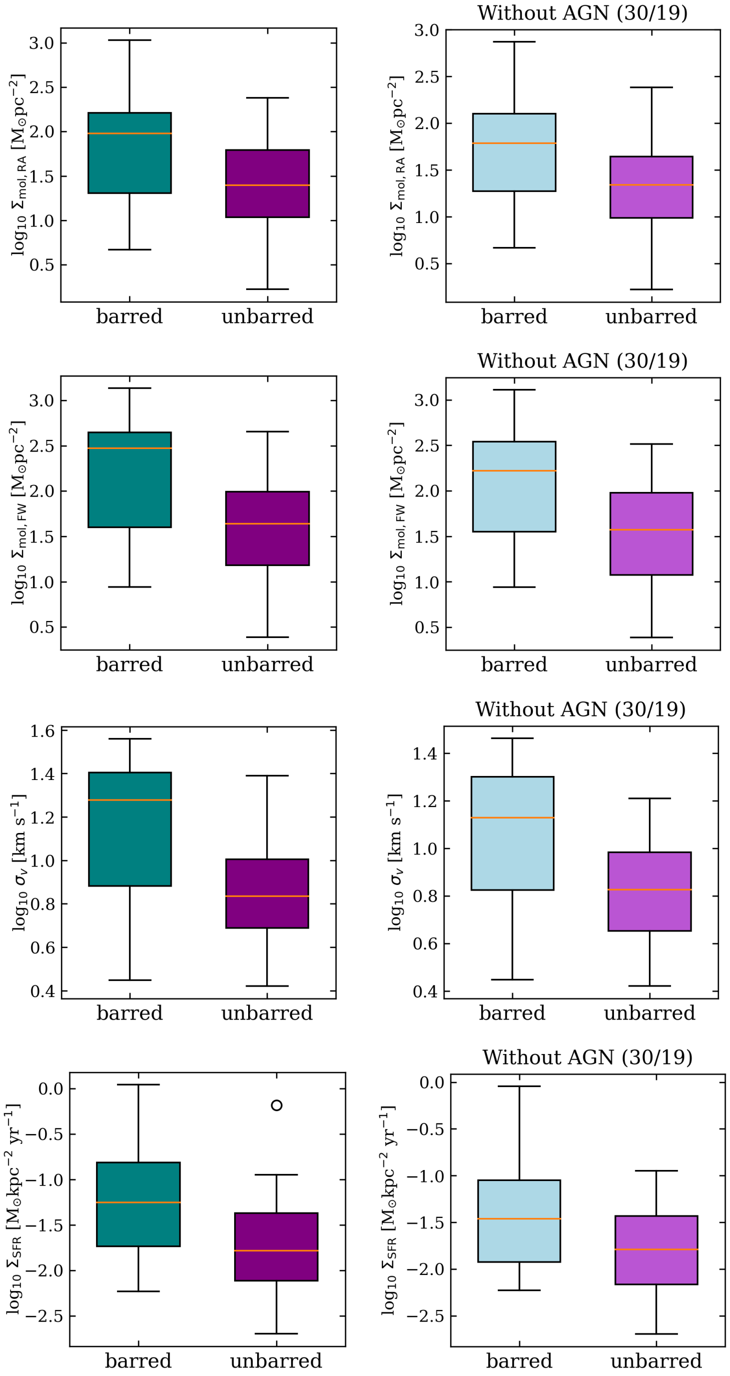

Figure 3.5 Boxplots showing the property distributions, comparing galaxies with the AGN included (left column as shown previously) with the AGN removed (right column). Each property is separated into barred (30) and unbarred (19) galaxies for the samples with no AGN.

populations. The $\Sigma_{\rm SFR}$ also has a slightly weaker statistic with p-value = 0.058. Barred galaxies with an AGN are found to be different than barred galaxies with no AGN, which is expected.

Figure 3.5 compares the new distributions of barred and unbarred galaxies with no AGN (right column) with the original sample that includes everything (left column). We can see the effect the AGN have of increasing the properties, especially for the barred distributions. Figure 3.6 shows the striking impact the AGN galaxies have on the distributions.

3.3.2 Linear Regression Results Excluding AGN

Table 3.5 shows the slopes and intercepts for the barred versus unbarred galaxy comparison for galaxies with no AGN. I want to highlight the Kennicutt-Schmidt relation which has a lower slope than what is found for the full sample with the AGN included. Figures 3.7 and 3.8 show the results of the Linmix linear regression. The top plot in Figure 3.7 shows the comparison between $\Sigma_{\rm mol,FW}$ and σ_v where the increase for barred galaxies is clear. The bottom plot in Figure 3.7 shows the comparison of σ_v with $\Sigma_{\rm SFR}$ for galaxies with no AGN. Figure 3.8 highlights where the AGN sit in both plots for just the barred galaxies. Given the differences seen in barred galaxies with AGN, it might be prudent to remove AGN hosts from our final analysis.

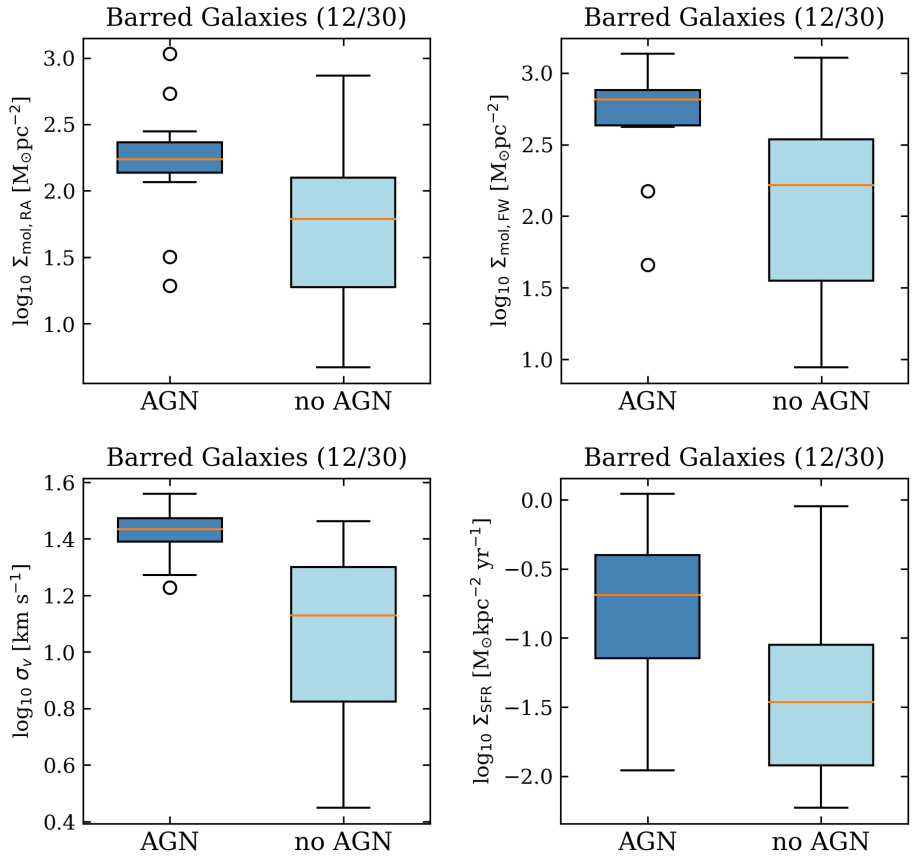

Figure 3.6 Boxplots showing the distributions of each individual sample. Each property is separated into barred galaxies with an AGN (12) and barred galaxies with no AGN (30).

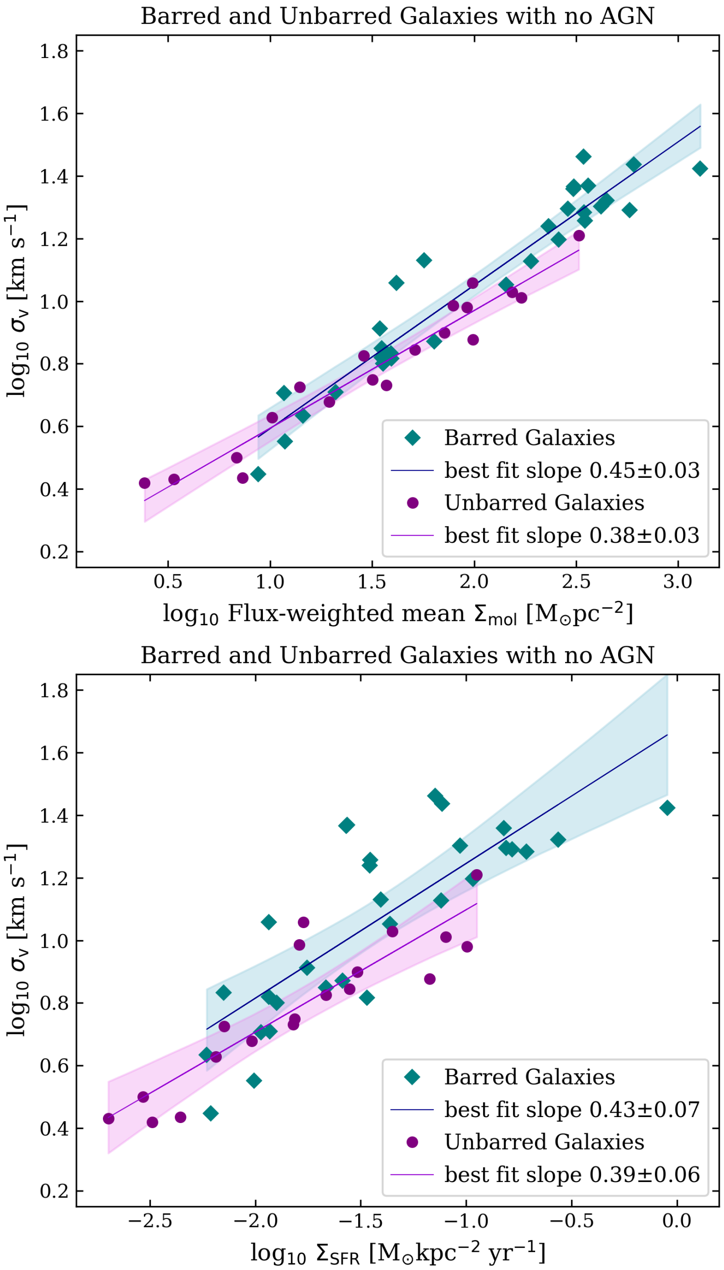

Figure 3.7 Barred versus unbarred resolved galaxy properties with no AGN. [Top] σ_v as a function of $\Sigma_{\rm mol,FW}$; [Bottom] σ_v as a function of $\Sigma_{\rm SFR}$. Best fit lines generated with Linmix with slope and intercept uncertainties shown in shaded regions. We still see an increase for barred galaxies in both plots.

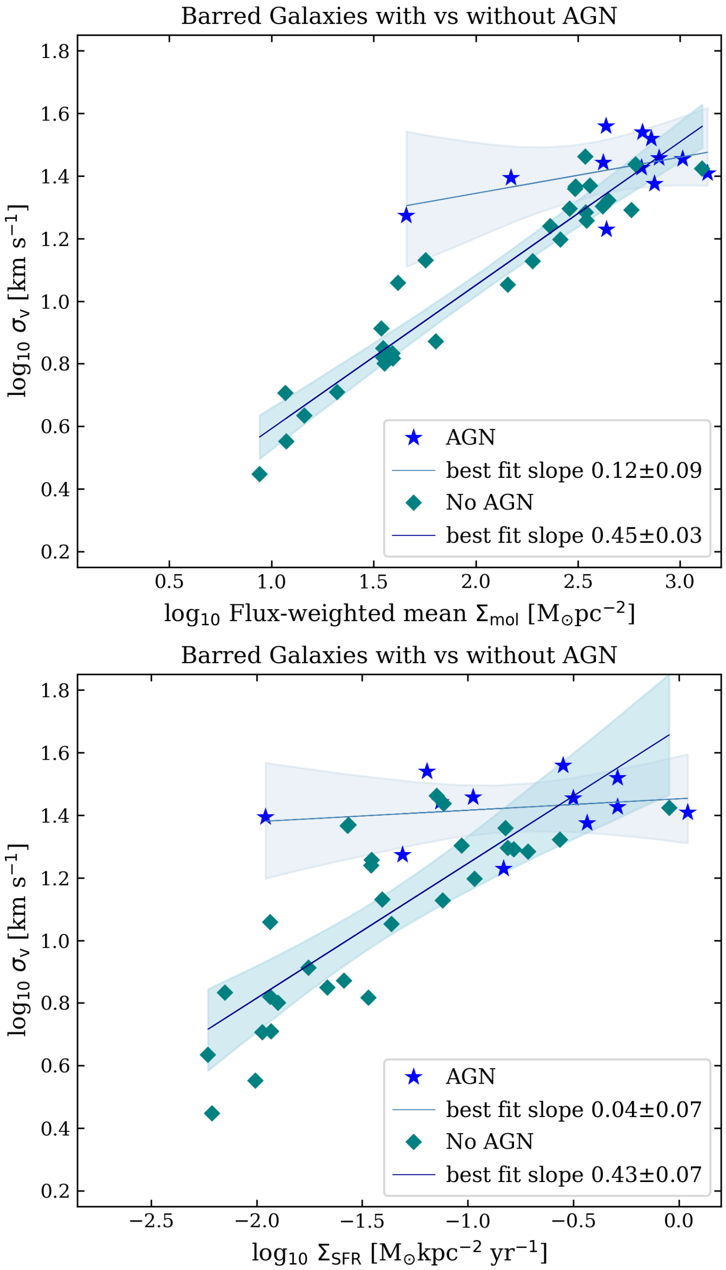

Figure 3.8 Resolved properties for barred galaxies with and without an AGN. [Top] σ_v as a function of $\Sigma_{\rm mol,FW}$; [Bottom] σ_v as a function of $\Sigma_{\rm SFR}$. Best fit lines generated with Linmix with slope and intercept uncertainties shown in shaded regions. This plot shows the higher values for galaxies with AGN, particularly σ_v.

Table 3.5 Statistical results of Linmix linear regression comparing 30 barred and 19 unbarred galaxies with no AGN for each comparison. In each case the resulting Linmix best fit slopes (with uncertainty) and intercepts (with uncertainty) are listed.

	Slope	
	Barred	**Unbarred**
$\Sigma_{\mathrm{mol,RA}}$ vs σ_v	0.46 ± 0.05	0.36 ± 0.05
$\Sigma_{\mathrm{mol,RW}}$ vs σ_v	0.46 ± 0.03	0.38 ± 0.03
$\Sigma_{\mathrm{mol,RA}}$ vs Σ_{SFR}	0.82 ± 0.10	0.84 ± 0.12
Σ_{SFR} vs σ_v	0.43 ± 0.07	0.39 ± 0.05
	Intercept	
	Barred	**Unbarred**
$\Sigma_{\mathrm{mol,RA}}$ vs σ_v	0.36 ± 0.05	0.31 ± 0.08
$\Sigma_{\mathrm{mol,RW}}$ vs σ_v	0.13 ± 0.06	0.22 ± 0.04
$\Sigma_{\mathrm{mol,RA}}$ vs Σ_{SFR}	-2.79 ± 0.17	-2.90 ± 0.17
Σ_{SFR} vs σ_v	1.68 ± 0.10	1.49 ± 0.10

3.4 Environment: Cluster versus Field

The environment where a galaxy is born plays an important role in the evolution of that galaxy. Galaxies falling into a cluster can have their gas striped away due to ram pressure stripping as the galaxy moves at high velocities through the hot cluster medium (Boselli and Gavazzi, 2014). We might expect the molecular gas to vary in galaxies in clusters versus those in the field. However, the centres may experience less of a change due to the higher potential well near the centre of the galaxy.

Once again I have compared the gas properties of barred and unbarred galaxies, this time looking at the effect of the external environment. My sample has galaxies in Virgo as well as Fornax and Eridanus. The original sample was divided up as follows with sample size shown in brackets:

1. Barred galaxies in a cluster (10)
2. Unbarred galaxies in a cluster (4)
3. Barred galaxies in the field (32)
4. Unbarred galaxies in the field (18)

I considered various comparisons again and noted that the sample of unbarred galaxies in a cluster is too small for the statistics to be informative. The two combinations I decided to study are barred and unbarred galaxies in the field, and barred galaxies in a cluster vs in the field. I performed the same AD-test and linear regression using Linmix and show these next.

3.4.1 Anderson-Darling Test Results – Environment

Table 3.6 shows the results of the AD-test for goodness-of-fit for the sample of barred versus unbarred galaxies that are not in a cluster as well as for the barred galaxies in a cluster versus in the field. Removing the effect of the cluster from the barred and unbarred galaxies does not change the results of the AD-test. They are still shown to be from different populations, except for depletion time. In addition, there is no difference found between barred galaxies in clusters versus those in the field.

Similar to the previous section, in Figure 3.9, I am comparing the new distributions of barred and unbarred galaxies in the field (right column) with the original sample that includes galaxies in clusters (left column). We can see that there is very little effect from the cluster on the gas properties in the galaxy centres. Figure 3.10 shows the cluster versus field distributions for barred galaxies.

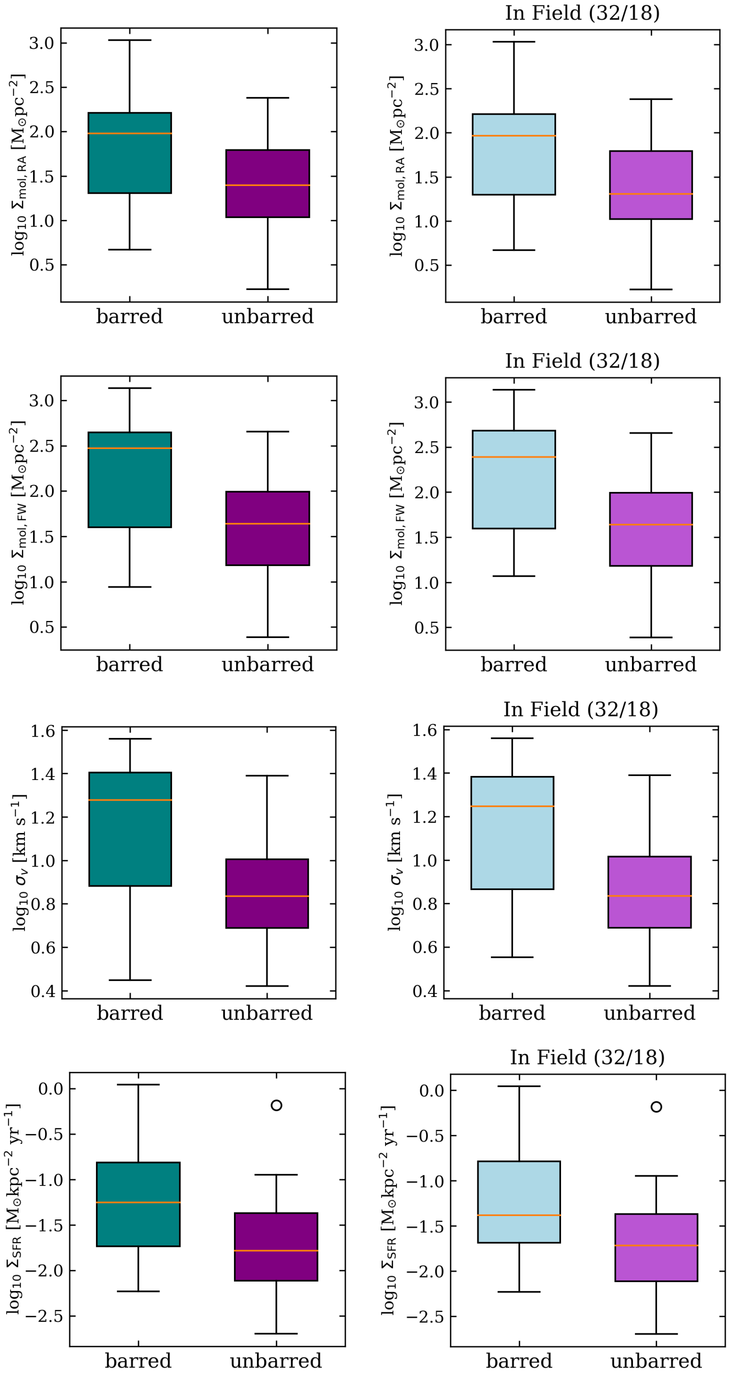

Figure 3.9 Boxplots showing the property distributions, comparing galaxies in both clusters and the field (left column as shown previously) and galaxies only in the field (right column). Each property is separated into barred (32) and unbarred (18) galaxies for the samples with no AGN.

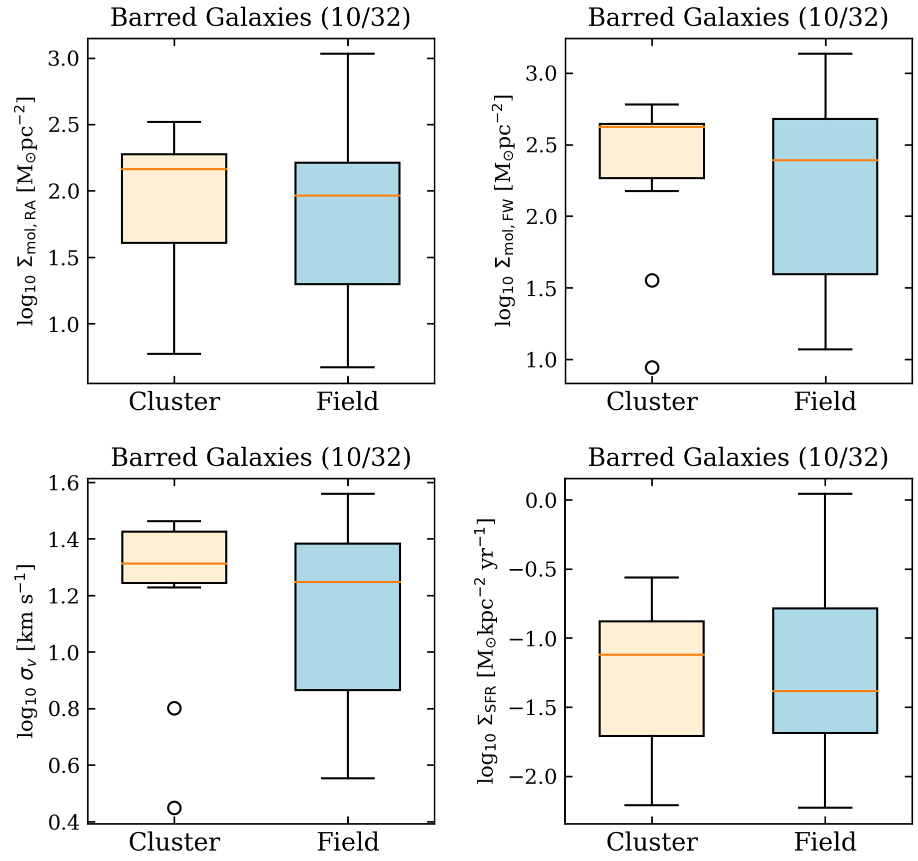

Figure 3.10 Boxplots showing the distributions of each individual sample. Each property is separated into barred galaxies in a cluster (10) and barred galaxies in the field (32).

Table 3.6 Statistical results of Anderson-Darling test for goodness-of-fit for the sample that considers environment around the galaxy, whether it is in a cluster or in the field. In each case the AD statistic, the p-value, and the evaluation are listed.

	Property	**AD statistic**	**p-value**	**evaluation**
Barred (32) vs Unbarred (18) (Field)	$\log \Sigma_{\mathrm{mol,RA}}$	2.5	0.03	●
	$\log \Sigma_{\mathrm{mol,FW}}$	4.1	0.0073	●
	σ_{v}	5.2	0.0028	●
	Σ_{SFR}	2.2	0.041	●
	t_{dep}	-0.09	0.39	+
Cluster (10) vs Field (32) (Barred galaxies)	$\log \Sigma_{\mathrm{mol,RA}}$	-0.69	0.77	+
	$\log \Sigma_{\mathrm{mol,FW}}$	-0.29	0.26	+
	σ_{v}	-0.37	0.54	+
	Σ_{SFR}	-0.50	0.63	+
	t_{dep}	1.02	0.12	+

3.4.2 Linear Regression Results – Environment

Table 3.7 shows the slopes and intercepts when comparing barred versus unbarred galaxies in the field. In this case, since the distributions do not vary a lot compared to the full sample, we see that the Kennicutt-Schmidt relation, for example, has a comparable slope of 0.90 ± 0.10. Figures 3.11 and 3.12 show the results of the linmix linear regression with uncertainty of the slopes in the shaded regions. We see the same increase in the properties for the barred galaxies for both plots in Figure 3.11. Figure 3.12 highlights where galaxies in clusters sit in both plots for just the barred galaxies. A larger sample size would be useful here for a better comparison since we only have 10 galaxies in clusters. This field galaxy analysis suggests that using both field and cluster galaxies together is fine for our main sample.

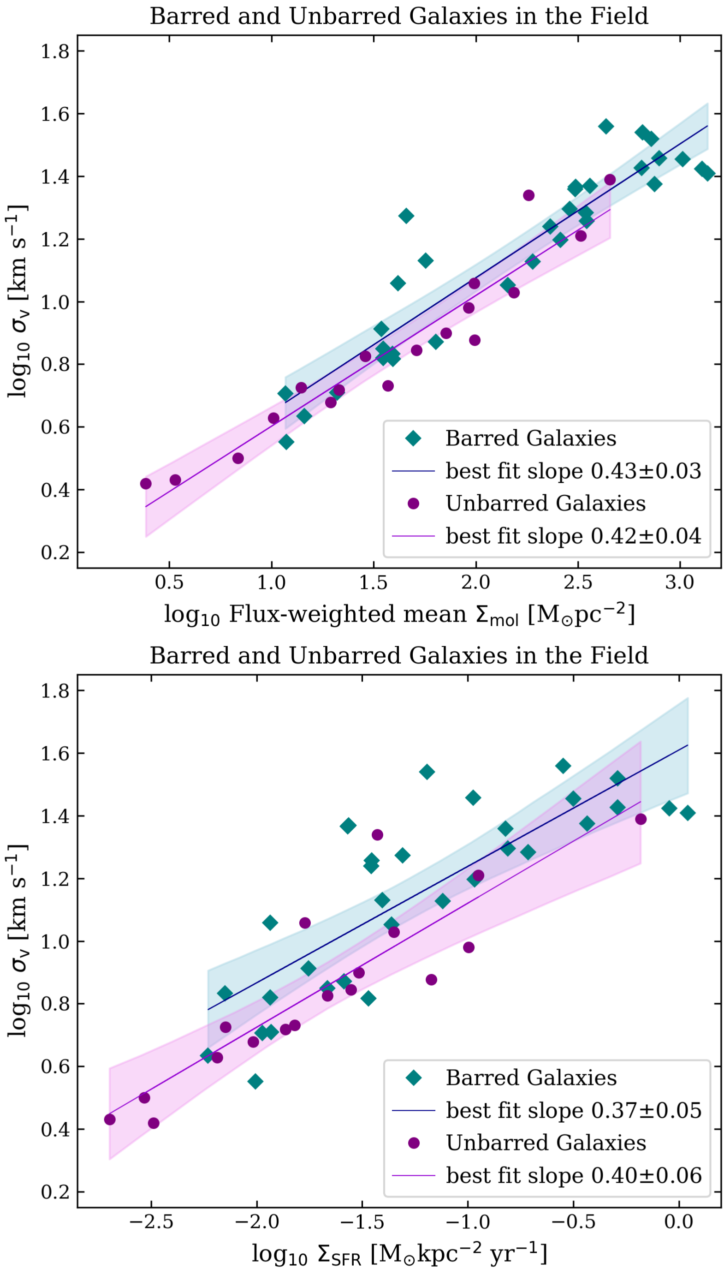

Figure 3.11 Barred versus unbarred resolved galaxy properties in the field. [Top] σ_v as a function of $\Sigma_{\rm mol,FW}$; [Bottom] σ_v as a function of $\Sigma_{\rm SFR}$. Best fit lines generated with Linmix with slope and intercept uncertainties shown in shaded regions. We still see an increase for barred galaxies in both plots, which do not vary compared to the full sample.

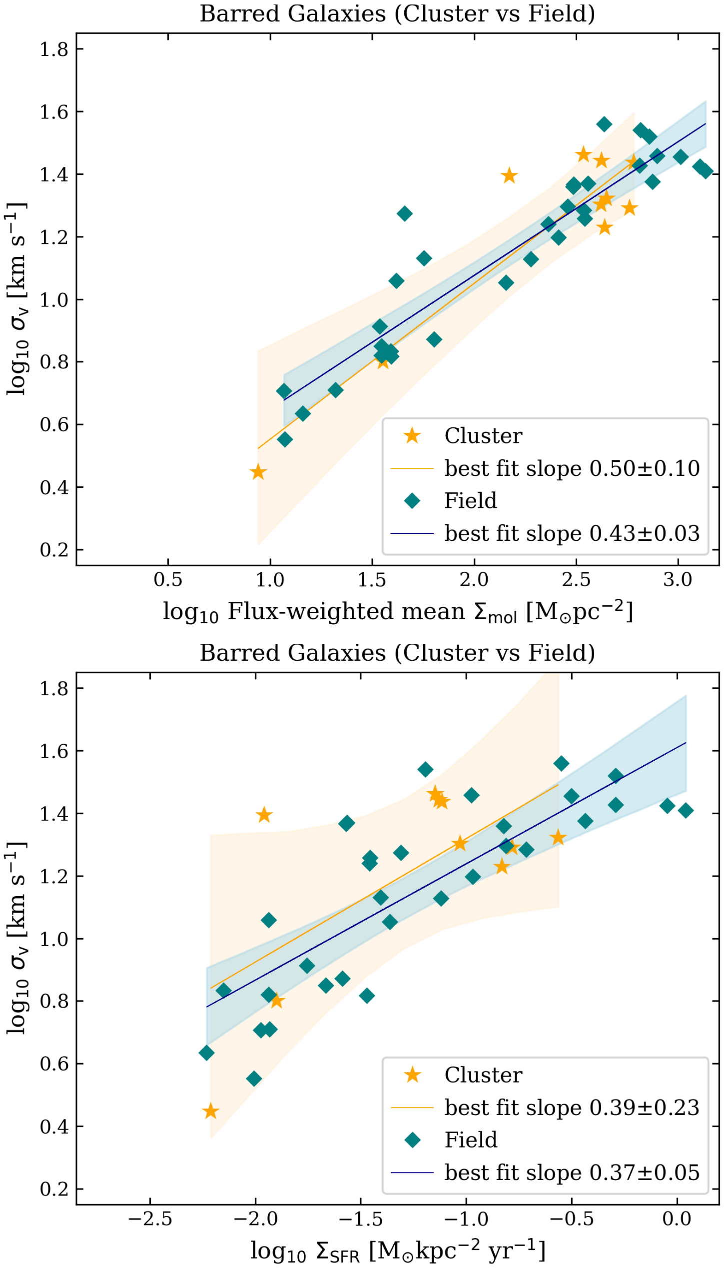

Figure 3.12 Resolved properties for galaxies in clusters versus in the field. [Top] σ_v as a function of $\Sigma_{\mathrm{mol,FW}}$; [Bottom] σ_v as a function of Σ_{SFR}. Best fit lines generated with Linmix with slope and intercept uncertainties shown in shaded regions. There is a lot of scatter in the cluster galaxies.

Table 3.7 Statistical results of Linmix linear regression comparing 32 barred and 18 unbarred galaxies in the field for each comparison. In each case the resulting Linmix best fit slopes (with uncertainty) and intercepts (with uncertainty) are listed.

	Slope	
	Barred	**Unbarred**
$\Sigma_{\mathrm{mol,RA}}$ vs σ_v	0.42 ± 0.05	0.42 ± 0.06
$\Sigma_{\mathrm{mol,RW}}$ vs σ_v	0.43 ± 0.03	0.42 ± 0.04
$\Sigma_{\mathrm{mol,RA}}$ vs Σ_{SFR}	0.90 ± 0.10	0.95 ± 0.14
Σ_{SFR} vs σ_v	0.37 ± 0.05	0.40 ± 0.07
	Intercept	
	Barred	**Unbarred**
$\Sigma_{\mathrm{mol,RA}}$ vs σ_v	0.40 ± 0.09	0.28 ± 0.09
$\Sigma_{\mathrm{mol,RW}}$ vs σ_v	0.22 ± 0.06	0.18 ± 0.06
$\Sigma_{\mathrm{mol,RA}}$ vs Σ_{SFR}	-2.86 ± 0.19	-2.97 ± 0.20
Σ_{SFR} vs σ_v	1.61 ± 0.07	1.52 ± 0.11

Chapter 4

Conclusion and Future Work

In this thesis I have carried out a statistical analysis of central molecular gas and star formation properties using high resolution, cloud-scale data and medium resolution SFR data from PHANGS. I found that molecular gas surface densities, velocity dispersions, and SFR surface densities are higher in barred galaxy centres. An Anderson-Darling statistical test for continuous distributions shows statistically significant differences between barred and unbarred galaxies for all three quantities.

Although the barred and unbarred galaxies are statistically different for $\Sigma_{\mathrm{mol,RA}}$ and Σ_{SFR} themselves, the fact that the two distributions for the molecular gas depletion time,

$$t_{\mathrm{dep}} = \frac{\Sigma_{\mathrm{mol,RA}}}{\Sigma_{\mathrm{SFR}}} \tag{4.0.1}$$

are the same is noteworthy. Figure 4.1 shows t_{dep} as a function of σ_v as well as the box plots for the two distributions. The AD-test gave a p-value of $p = 0.34$, from Table 3.2, for the t_{dep} for the full sample. We see that t_{dep} is within the expected range of approximately $1 - 3$ Gyr for the molecular gas in spiral galaxies (Querejeta

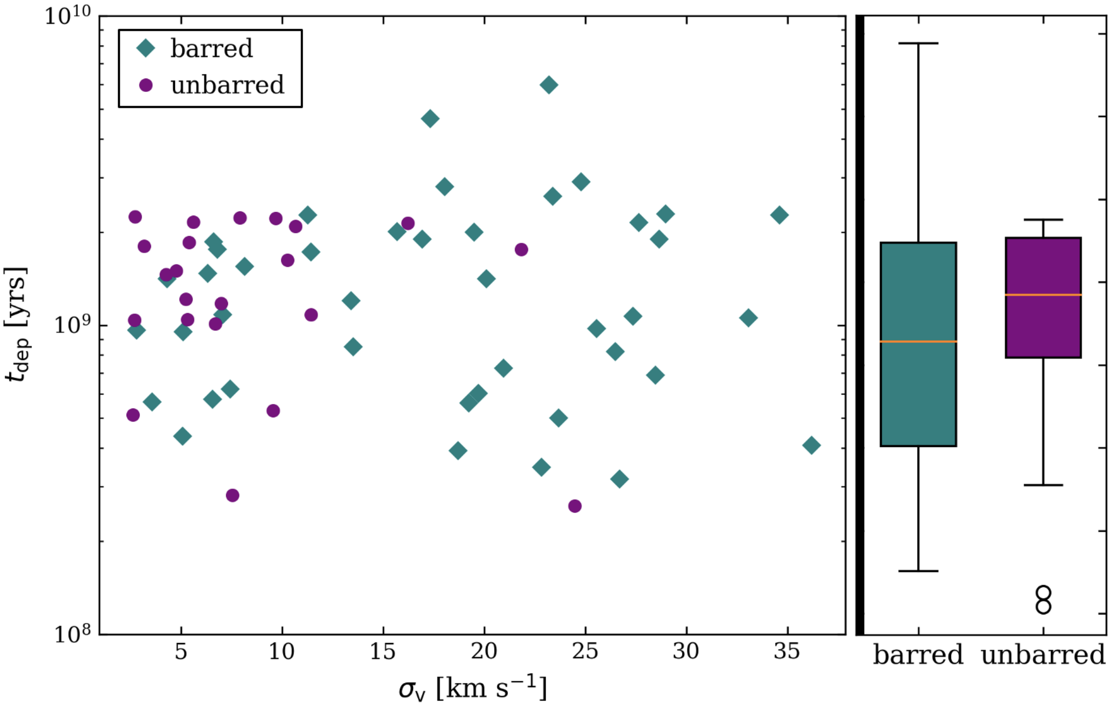

Figure 4.1 Molecular gas depletion time, $t_{\rm dep}$, as a function of molecular velocity dispersion, σ_v. On the right are box plots of $t_{\rm dep}$ for barred and unbarred galaxies. $t_{\rm dep}$ is within the range of approximately $1 - 3$ Gyr.

et al., 2021). It would be an interesting test to see if we find the same thing for the other two ratios of the quantities investigated in this thesis, namely:

$$\frac{\sigma_v}{\Sigma_{\mathrm{mol,FW}}} \text{ and } \frac{\sigma_v}{\Sigma_{\mathrm{SFR}}}. \tag{4.0.2}$$

A statistical test of these two new ratios is worthwhile because they compare the properties which first inspired this thesis, σ_v and $\Sigma_{\mathrm{mol,FW}}$, which were both higher in barred galaxies, as well as the less well studied relation between σ_v and Σ_{SFR}. This would be part of some follow up work on my thesis.

Unfortunately, the cluster galaxy sample was too small to compare large scale environments. Connecting the effects of the large scale environment with the macro-structure inside the galaxy (bar, centre, arm, versus outer arm regions) and then in turn with cloud-scale physics within each of these regions is an important next step for understanding galaxy evolution. In my future research, I plan to quantify links between cloud-scale physics and cluster-scale environment and measure how these links change the star formation rates across entire galaxies and in subgalactic regions. My analysis will probe variations in molecular cloud physical properties (such as mass, dynamical state, and evolutionary timescales) by comparing galaxies in the Virgo Cluster with field galaxies as a control sample. Broadening the region of interest from centres to entire galactic disks will allow me to analyze the environmental influences on gas properties in different parts of the galaxy.

Extensive work has been done to explore the effects of the external environment on galaxy evolution at kpc resolutions. The collaboration team for the Virgo Environment Traced in CO (VERTICO) survey analyzed a sample of 51 Virgo Cluster galaxies and found that Virgo galaxies with reduced gas mass have proportionally lower Σ_{SFR} and Σ_{mol}, but systematic changes as ram pressure stripping progresses (Brown et al., 2023). A natural next question after the work done by VERTICO is to determine how these systematic changes on kiloparsec scales stem from changes in molecular cloud properties on $<\sim$ 100 pc scales.

The star formation rate data used in this thesis were medium resolution, not cloud scale resolution like the other properties $\Sigma_{\mathrm{mol,FW}}$ and σ_v in the PHANGS data. In my future research I will make use of data from a new large program, MUSE and ALMA Unveiling the Virgo Environment (MAUVE) which matches two surveys at different wavelengths. First, a new ALMA high resolution survey of 40 Virgo cluster galaxies at unprecedented 50 pc resolution (PI: J. Sun) will begin to collect data in 2024. This high resolution data is needed to answer ongoing questions about the effect of environment on the ISM at smaller scales. The second part of MAUVE is the MUSE large program which has begun data collection as of 2023 (PI: L. Cortese). With this data, I will obtain $\sim$100 pc scale ionized gas excitation and SFR maps. By comparing emission line measurements from these observations I will be able to determine if the gas is excited by star formation or another source such as shocks. The PHANGS survey (Leroy et al., 2021b) of 90 nearby galaxies is made up of mostly field galaxies and will be an excellent control sample to compare with these new measurements in Virgo Cluster galaxies. My planned research will represent a step forward in understanding the interactions between cloud-scale physics and the large-scale environment and how these impact the evolution of galaxies.

Bibliography

M. R. Blanton and J. Moustakas. Physical Properties and Environments of Nearby Galaxies. *ARA&A*, 47(1):159–210, Sept. 2009. doi: 10.1146/annurev-astro-082708-101734.

A. D. Bolatto, A. K. Leroy, E. Rosolowsky, F. Walter, and L. Blitz. The Resolved Properties of Extragalactic Giant Molecular Clouds. *ApJ*, 686(2):948–965, Oct. 2008. doi: 10.1086/591513.

A. D. Bolatto, M. Wolfire, and A. K. Leroy. The CO-to-H_2 Conversion Factor. *ARA&A*, 51(1):207–268, Aug. 2013. doi: 10.1146/annurev-astro-082812-140944.

A. D. Bolatto, A. K. Leroy, R. C. Levy, D. S. Meier, E. A. C. Mills, T. A. Thompson, K. L. Emig, S. Veilleux, J. Ott, M. Gorski, F. Walter, L. A. Lopez, and L. Lenkić. ALMA Imaging of a Galactic Molecular Outflow in NGC 4945. *ApJ*, 923(1):83, Dec. 2021. doi: 10.3847/1538-4357/ac2c08.

A. Boselli and G. Gavazzi. Environmental Effects on Late-Type Galaxies in Nearby Clusters. *PASP*, 118(842):517–559, Apr. 2006. doi: 10.1086/500691.

A. Boselli and G. Gavazzi. On the origin of the faint-end of the red sequence in high-density environments. *A&AR*, 22:74, Nov. 2014. doi: 10.1007/s00159-014-0074-y.

T. Brown, C. D. Wilson, N. Zabel, T. A. Davis, A. Boselli, A. Chung, S. L. Ellison, C. D. P. Lagos, A. R. H. Stevens, L. Cortese, Y. M. Bahé, D. Bisaria, A. D. Bolatto, C. R. Cashmore, B. Catinella, R. Chown, B. Diemer, P. J. Elahi, M. H. Hani, M. J. Jiménez-Donaire, B. Lee, K. Leidig, A. Mok, K. P. Olsen, L. C. Parker, I. D. Roberts, R. Smith, K. Spekkens, M. Thorp, S. Tonnesen, E. Vienneau, V. Villanueva, S. N. Vogel, J. Wadsley, C. Welker, and H. Yoon. VERTICO: The Virgo Environment Traced in CO Survey. *ApJS*, 257(2):21, Dec. 2021. doi: 10.3847/1538-4365/ac28f5.

T. Brown, I. D. Roberts, M. Thorp, S. L. Ellison, N. Zabel, C. D. Wilson, Y. M. Bahé, D. Bisaria, A. D. Bolatto, A. Boselli, A. Chung, L. Cortese, B. Catinella, T. A. Davis, M. J. Jiménez-Donaire, C. D. P. Lagos, B. Lee, L. C. Parker, R. Smith, K. Spekkens, A. R. H. Stevens, V. Villanueva, and A. B. Watts. VERTICO VII: Environmental quenching caused by suppression of molecular gas content and star formation efficiency in Virgo Cluster galaxies. *arXiv e-prints*, art. arXiv:2308.10943, Aug. 2023. doi: 10.48550/arXiv.2308.10943.

N. Brunetti, C. D. Wilson, K. Sliwa, E. Schinnerer, S. Aalto, and A. B. Peck. Highly turbulent gas on GMC scales in NGC 3256, the nearest luminous infrared galaxy. *MNRAS*, 500(4):4730–4748, Jan. 2021. doi: 10.1093/mnras/staa3425.

M. Chevance, M. R. Krumholz, A. F. McLeod, E. C. Ostriker, E. W. Rosolowsky, and A. Sternberg. The Life and Times of Giant Molecular Clouds. In S. Inutsuka, Y. Aikawa, T. Muto, K. Tomida, and M. Tamura, editors, *Protostars and Planets VII*, volume 534 of *Astronomical Society of the Pacific Conference Series*, page 1, July 2023. doi: 10.48550/arXiv.2203.09570.

F. Combes. AGN fueling and feedback, from pc to kpc scale. *arXiv e-prints*, art. arXiv:1911.00707, Nov. 2019. doi: 10.48550/arXiv.1911.00707.

F. Combes, S. García-Burillo, A. Audibert, L. Hunt, A. Eckart, S. Aalto, V. Casasola, F. Boone, M. Krips, S. Viti, K. Sakamoto, S. Muller, K. Dasyra, P. van der Werf, and S. Martin. ALMA observations of molecular tori around massive black holes. *A&A*, 623:A79, Mar. 2019. doi: 10.1051/0004-6361/201834560.

L. Cortese, B. Catinella, S. Boissier, A. Boselli, and S. Heinis. The effect of the environment on the H I scaling relations. *MNRAS*, 415(2):1797–1806, Aug. 2011. doi: 10.1111/j.1365-2966.2011.18822.x.

L. Cortese, B. Catinella, and R. Smith. The Dawes Review 9: The role of cold gas stripping on the star formation quenching of satellite galaxies. *PASA*, 38:e035, Aug. 2021. doi: 10.1017/pasa.2021.18.

T. Costa, D. Sijacki, and M. G. Haehnelt. Feedback from active galactic nuclei: energy- versus momentum-driving. *MNRAS*, 444(3):2355–2376, Nov. 2014. doi: 10.1093/mnras/stu1632.

G. de Vaucouleurs. Revised Classification of 1500 Bright Galaxies. *ApJS*, 8:31, Apr. 1963. doi: 10.1086/190084.

S. Díaz-García, F. D. Moyano, S. Comerón, J. H. Knapen, H. Salo, and A. Y. K. Bouquin. Distribution of star formation in galactic bars as seen with Hα and stacked GALEX UV imaging. *A&A*, 644:A38, Dec. 2020. doi: 10.1051/0004-6361/202039162.

S. Díaz-García, U. Lisenfeld, I. Pérez, A. Zurita, S. Verley, F. Combes, D. Espada, S. Leon, V. Martínez-Badenes, J. Sabater, and L. Verdes-Montenegro. Molecular gas and star formation within 12 strong galactic bars observed with IRAM-30 m. *A&A*, 654:A135, Oct. 2021. doi: 10.1051/0004-6361/202140674.

L. Ferrarese, P. Côté, J.-C. Cuillandre, S. D. J. Gwyn, E. W. Peng, L. A. MacArthur, P.-A. Duc, A. Boselli, S. Mei, T. Erben, A. W. McConnachie, P. R. Durrell, J. C. Mihos, A. Jordán, A. Lançon, T. H. Puzia, E. Emsellem, M. L. Balogh, J. P. Blakeslee, L. van Waerbeke, R. Gavazzi, B. Vollmer, J. J. Kavelaars, D. Woods, N. M. Ball, S. Boissier, S. Courteau, E. Ferriere, G. Gavazzi, H. Hildebrandt, P. Hudelot, M. Huertas-Company, C. Liu, D. McLaughlin, Y. Mellier, M. Milkeraitis, D. Schade, C. Balkowski, F. Bournaud, R. G. Carlberg, S. C. Chapman, H. Hoekstra, C. Peng, M. Sawicki, L. Simard, J. E. Taylor, R. B. Tully, W. van Driel, C. D. Wilson, T. Burdullis, B. Mahoney, and N. Manset. The Next Generation Virgo Cluster Survey (NGVS). I. Introduction to the Survey. *ApJS*, 200(1):4, May 2012. doi: 10.1088/0067-0049/200/1/4.

E. Habart, M. Walmsley, L. Verstraete, S. Cazaux, R. Maiolino, P. Cox, F. Boulanger, and G. Pineau des Forêts. Molecular Hydrogen. *SSR*, 119(1-4):71–91, Aug. 2005. doi: 10.1007/s11214-005-8062-1.

M. P. Haynes and R. Giovanelli. Neutral hydrogen in isolated galaxies. IV. Results for the Arecibo sample. *AJ*, 89:758–800, June 1984. doi: 10.1086/113573.

M. H. Heyer and C. Brunt. Turbulence in the molecular interstellar medium. In B. G. Elmegreen and J. Palous, editors, *Triggered Star Formation in a Turbulent ISM*, volume 237, pages 9–16, Jan. 2007. doi: 10.1017/S1743921307001159.

M. H. Heyer, J. M. Carpenter, and R. L. Snell. The Equilibrium State of Molecular Regions in the Outer Galaxy. *ApJ*, 551(2):852–866, Apr. 2001. doi: 10.1086/320218.

L. K. Hunt, S. García-Burillo, V. Casasola, P. Caselli, F. Combes, C. Henkel, A. Lundgren, R. Maiolino, K. M. Menten, L. Testi, and A. Weiss. Molecular depletion times and the CO-to-H_2 conversion factor in metal-poor galaxies. *A&A*, 583:A114, Nov. 2015. doi: 10.1051/0004-6361/201526553.

M. J. Jiménez-Donaire, T. Brown, C. D. Wilson, I. D. Roberts, N. Zabel, S. L. Ellison, M. Thorp, V. Villanueva, R. Chown, D. Bisaria, A. D. Bolatto, A. Boselli, B. Catinella, A. Chung, L. Cortese, T. A. Davis, C. D. P. Lagos, B. Lee, L. C. Parker, K. Spekkens, A. R. H. Stevens, and J. Sun. VERTICO. III. The Kennicutt-Schmidt relation in Virgo cluster galaxies. *A&A*, 671:A3, Mar. 2023. doi: 10.1051/0004-6361/202244718.

S. Jogee, F. D. Barazza, H.-W. Rix, I. Shlosman, M. Barden, C. Wolf, J. Davies, I. Heyer, S. V. W. Beckwith, E. F. Bell, A. Borch, J. A. R. Caldwell, C. J. Conselice, T. Dahlen, B. Häussler, C. Heymans, K. Jahnke, J. H. Knapen, S. Laine, G. M. Lubell, B. Mobasher, D. H. McIntosh, K. Meisenheimer, C. Y. Peng, S. Ravindranath, S. F. Sanchez, R. S. Somerville, and L. Wisotzki. Bar Evolution over the Last 8 Billion Years: A Constant Fraction of Strong Bars in the GEMS Survey. *ApJL*, 615(2):L105–L108, Nov. 2004. doi: 10.1086/426138.

S. Jogee, N. Scoville, and J. D. P. Kenney. The Central Region of Barred Galaxies: Molecular Environment, Starbursts, and Secular Evolution. *ApJL*, 630(2):837–863, Sept. 2005. doi: 10.1086/432106.

J. Kennicutt, Robert C. The Star Formation Law in Galactic Disks. *ApJ*, 344:685, Sept. 1989. doi: 10.1086/167834.

R. C. Kennicutt and N. J. Evans. Star Formation in the Milky Way and Nearby Galaxies. *ARA&A*, 50:531–608, Sept. 2012. doi: 10.1146/annurev-astro-081811-125610.

R. A. Koopmann and J. D. P. Kenney. Massive Star Formation Rates and Radial Distributions from Hα Imaging of 84 Virgo Cluster and Isolated Spiral Galaxies. *ApJ*, 613(2):851–865, Oct. 2004. doi: 10.1086/423190.

J. Kormendy and J. Kennicutt, Robert C. Secular Evolution and the Formation of Pseudobulges in Disk Galaxies. *ARA&A*, 42(1):603–683, Sept. 2004. doi: 10.1146/annurev.astro.42.053102.134024.

M. R. Krumholz. Star Formation and Gas Dynamics of the Central Molecular Zone. In M. Tsuboi and T. Oka, editors, *New Horizons in Galactic Center Astronomy and Beyond*, volume 528 of *Astronomical Society of the Pacific Conference Series*, page 19, July 2021.

M. R. Krumholz, B. Burkhart, J. C. Forbes, and R. M. Crocker. A unified model for galactic discs: star formation, turbulence driving, and mass transport. *MNRAS*, 477(2):2716–2740, June 2018. doi: 10.1093/mnras/sty852.

A. K. Leroy, C. Lee, A. Schruba, A. Bolatto, A. Hughes, J. Pety, K. Sandstrom, E. Schinnerer, and F. Walter. Clumping and the Interpretation of kpc-scale Maps of the Interstellar Medium: Smooth H I and Clumpy, Variable H_2 Surface Density. *ApJ*, 769(1):L12, May 2013a. doi: 10.1088/2041-8205/769/1/L12.

A. K. Leroy, F. Walter, K. Sandstrom, A. Schruba, J.-C. Munoz-Mateos, F. Bigiel, A. Bolatto, E. Brinks, W. J. G. de Blok, S. Meidt, H.-W. Rix, E. Rosolowsky, E. Schinnerer, K.-F. Schuster, and A. Usero. Molecular Gas and Star Formation in nearby Disk Galaxies. *ApJ*, 146(2):19, Aug. 2013b. doi: 10.1088/0004-6256/146/2/19.

A. K. Leroy, K. M. Sandstrom, D. Lang, A. Lewis, S. Salim, E. A. Behrens, J. Chastenet, I.-D. Chiang, M. J. Gallagher, S. Kessler, and D. Utomo. A z = 0 Multiwavelength Galaxy Synthesis. I. A WISE and GALEX Atlas of Local Galaxies. *ApJS*, 244(2):24, Oct. 2019. doi: 10.3847/1538-4365/ab3925.

A. K. Leroy, A. Hughes, D. Liu, J. Pety, E. Rosolowsky, T. Saito, E. Schinnerer, A. Schruba, A. Usero, C. M. Faesi, C. N. Herrera, M. Chevance, A. P. S. Hygate, A. A. Kepley, E. W. Koch, M. Querejeta, K. Sliwa, D. Will, C. D. Wilson, G. S. Anand, A. Barnes, F. Belfiore, I. Bešlić, F. Bigiel, G. A. Blanc, A. D. Bolatto, M. Boquien, Y. Cao, R. Chandar, J. Chastenet, I.-D. Chiang, E. Congiu, D. A. Dale, S. Deger, J. S. den Brok, C. Eibensteiner, E. Emsellem, A. García-Rodríguez, S. C. O. Glover, K. Grasha, B. Groves, J. D. Henshaw, M. J. Jiménez Donaire, J. Kim, R. S. Klessen, K. Kreckel, J. M. D. Kruijssen, K. L. Larson, J. C. Lee, N. Mayker, R. McElroy, S. E. Meidt, A. Mok, H.-A. Pan, J. Puschnig, A. Razza, P. Sánchez-Bl'azquez, K. M. Sandstrom, F. Santoro, A. Sardone, F. Scheuermann, J. Sun, D. A. Thilker, J. A. Turner, L. Ubeda, D. Utomo, E. J. Watkins, and T. G. Williams. PHANGS-ALMA Data Processing and Pipeline. *ApJS*, 255(1):19, July 2021a. doi: 10.3847/1538-4365/abec80.

A. K. Leroy, E. Schinnerer, A. Hughes, E. Rosolowsky, J. Pety, A. Schruba, A. Usero,

G. A. Blanc, M. Chevance, E. Emsellem, C. M. Faesi, C. N. Herrera, D. Liu, S. E. Meidt, M. Querejeta, T. Saito, K. M. Sandstrom, J. Sun, T. G. Williams, G. S. Anand, A. T. Barnes, E. A. Behrens, F. Belfiore, S. M. Benincasa, I. Bešlić, F. Bigiel, A. D. Bolatto, J. S. den Brok, Y. Cao, R. Chandar, J. Chastenet, I.-D. Chiang, E. Congiu, D. A. Dale, S. Deger, C. Eibensteiner, O. V. Egorov, A. García-Rodríguez, S. C. O. Glover, K. Grasha, J. D. Henshaw, I. T. Ho, A. A. Kepley, J. Kim, R. S. Klessen, K. Kreckel, E. W. Koch, J. M. D. Kruijssen, K. L. Larson, J. C. Lee, L. A. Lopez, J. Machado, N. Mayker, R. McElroy, E. J. Murphy, E. C. Ostriker, H.-A. Pan, I. Pessa, J. Puschnig, A. Razza, P. Sánchez-Blázquez, F. Santoro, A. Sardone, F. Scheuermann, K. Sliwa, M. C. Sormani, S. K. Stuber, D. A. Thilker, J. A. Turner, D. Utomo, E. J. Watkins, and B. Whitmore. PHANGS-ALMA: Arcsecond CO(2-1) Imaging of Nearby Star-forming Galaxies. *ApJS*, 257 (2):43, Dec. 2021b. doi: 10.3847/1538-4365/ac17f3.

D. Liu, E. Schinnerer, T. Saito, E. Rosolowsky, A. Leroy, A. Usero, K. Sandstrom, R. S. Klessen, S. C. O. Glover, Y. Ao, I. Bešlić, F. Bigiel, Y. Cao, J. Chastenet, M. Chevance, D. A. Dale, Y. Gao, A. Hughes, K. Kreckel, J. M. D. Kruijssen, H.-A. Pan, J. Pety, D. Salak, F. Santoro, A. Schruba, J. Sun, Y.-H. Teng, and T. Williams. C I and CO in nearby spiral galaxies. I. Line ratio and abundance variations at ~200 pc scales. *A&A*, 672:A36, Apr. 2023. doi: 10.1051/0004-6361/202244564.

F. Maeda, F. Egusa, K. Ohta, Y. Fujimoto, A. Habe, and Y. Asada. CO(2-1)/CO(1-0) Line Ratio on a 100 Parsec Scale in the Nearby Barred Galaxy NGC 1300. *ApJ*, 926(1):96, Feb. 2022. doi: 10.3847/1538-4357/ac4505.

F. Maeda, F. Egusa, K. Ohta, Y. Fujimoto, and A. Habe. Statistical Study of the Star Formation Efficiency in Bars: Is Star Formation Suppressed in Gas-rich Bars? *ApJ*, 943(1):7, Jan. 2023. doi: 10.3847/1538-4357/aca664.

R. Maiolino, H. R. Russell, A. C. Fabian, S. Carniani, R. Gallagher, S. Cazzoli, S. Arribas, F. Belfiore, E. Bellocchi, L. Colina, G. Cresci, W. Ishibashi, A. Marconi, F. Mannucci, E. Oliva, and E. Sturm. Star formation inside a galactic outflow. *Nat*, 544(7649):202–206, Mar. 2017. doi: 10.1038/nature21677.

D. C. Martin, J. Fanson, D. Schiminovich, P. Morrissey, P. G. Friedman, T. A. Barlow, T. Conrow, R. Grange, P. N. Jelinsky, B. Milliard, O. H. W. Siegmund, L. Bianchi, Y.-I. Byun, J. Donas, K. Forster, T. M. Heckman, Y.-W. Lee, B. F. Madore, R. F. Malina, S. G. Neff, R. M. Rich, T. Small, F. Surber, A. S. Szalay, B. Welsh, and T. K. Wyder. The Galaxy Evolution Explorer: A Space Ultraviolet Survey Mission. *ApJL*, 619(1):L1–L6, Jan. 2005. doi: 10.1086/426387.

C. F. McKee and E. C. Ostriker. Theory of Star Formation. *ARA&A*, 45(1):565–687, Sept. 2007. doi: 10.1146/annurev.astro.45.051806.110602.

M. Querejeta, E. Schinnerer, S. Meidt, J. Sun, A. K. Leroy, E. Emsellem, R. S. Klessen, J. C. Muñoz-Mateos, H. Salo, E. Laurikainen, I. Bešlić, G. A. Blanc, M. Chevance, D. A. Dale, C. Eibensteiner, C. Faesi, A. García-Rodríguez, S. C. O. Glover, K. Grasha, J. Henshaw, C. Herrera, A. Hughes, K. Kreckel, J. M. D. Kruijssen, D. Liu, E. J. Murphy, H. A. Pan, J. Pety, A. Razza, E. Rosolowsky, T. Saito, A. Schruba, A. Usero, E. J. Watkins, and T. G. Williams. Stellar structures, molecular gas, and star formation across the PHANGS sample of nearby galaxies. *A&A*, 656:A133, Dec. 2021. doi: 10.1051/0004-6361/202140695.

M. W. Regan, M. D. Thornley, S. N. Vogel, K. Sheth, B. T. Draine, D. J. Hollenbach, M. Meyer, D. A. Dale, C. W. Engelbracht, R. C. Kennicutt, L. Armus, B. Buckalew, D. Calzetti, K. D. Gordon, G. Helou, C. Leitherer, S. Malhotra, E. Murphy, G. H. Rieke, M. J. Rieke, and J. D. Smith. The Radial Distribution of the Interstellar Medium in Disk Galaxies: Evidence for Secular Evolution. *ApJ*, 652(2):1112–1121, Dec. 2006. doi: 10.1086/505382.

E. Rosolowsky, A. Hughes, A. K. Leroy, J. Sun, M. Querejeta, A. Schruba, A. Usero, C. N. Herrera, D. Liu, J. Pety, T. Saito, I. Bešlić, F. Bigiel, G. Blanc, M. Chevance, D. A. Dale, S. Deger, C. M. Faesi, S. C. O. Glover, J. D. Henshaw, R. S. Klessen, J. M. D. Kruijssen, K. Larson, J. Lee, S. Meidt, A. Mok, E. Schinnerer, D. A. Thilker, and T. G. Williams. Giant molecular cloud catalogues for PHANGS-ALMA: methods and initial results. *MNRAS*, 502(1):1218–1245, Mar. 2021. doi: 10.1093/mnras/stab085.

K. Sakamoto, S. K. Okumura, S. Ishizuki, and N. Z. Scoville. Bar-driven Transport of Molecular Gas to Galactic Centers and Its Consequences. *ApJ*, 525(2):691–701, Nov. 1999. doi: 10.1086/307910.

E. Schinnerer, A. Hughes, A. Leroy, B. Groves, G. A. Blanc, K. Kreckel, F. Bigiel, M. Chevance, D. Dale, E. Emsellem, C. Faesi, S. Glover, K. Grasha, J. Henshaw, A. Hygate, J. M. D. Kruijssen, S. Meidt, J. Pety, M. Querejeta, E. Rosolowsky, T. Saito, A. Schruba, J. Sun, and D. Utomo. The Gas-Star Formation Cycle in Nearby Star-forming Galaxies. I. Assessment of Multi-scale Variations. *ApJ*, 887 (1):49, Dec. 2019. doi: 10.3847/1538-4357/ab50c2.

F. W. Scholz and M. A. Stephens. K-Sample Anderson–Darling Tests. *Journal of the American Statistical Association*, 82(399):918–924, Mar. 1987. doi: 10.1080/01621459.1987.10478517. URL `http://dx.doi.org/10.1080/01621459.1987.10478517`.

A. Schruba, A. K. Leroy, J. M. D. Kruijssen, F. Bigiel, A. D. Bolatto, W. J. G. de Blok, L. Tacconi, E. F. van Dishoeck, and F. Walter. Physical Properties of Molecular Clouds at 2 pc Resolution in the Low-metallicity Dwarf Galaxy NGC 6822 and the Milky Way. *ApJ*, 835(2):278, Feb. 2017. doi: 10.3847/1538-4357/835/2/278.

K. Sheth, S. N. Vogel, M. W. Regan, P. J. Teuben, A. I. Harris, and M. D. Thornley. Molecular Gas and Star Formation in Bars of Nearby Spiral Galaxies. *ApJ*, 124(5): 2581–2599, Nov. 2002a. doi: 10.1086/343835.

K. Sheth, S. N. Vogel, P. J. Teuben, A. I. Harris, M. W. Regan, M. D. Thornley, and T. T. Helfer. Comparing Molecular Gas and Star Formation Properties in the Central Regions of Barred and Unbarred Spirals. In E. Athanassoula, A. Bosma, and R. Mujica, editors, *Disks of Galaxies: Kinematics, Dynamics and Peturbations*, volume 275 of *Astronomical Society of the Pacific Conference Series*, pages 263–266, Dec. 2002b.

K. Sheth, M. Regan, J. L. Hinz, A. Gil de Paz, K. Menéndez-Delmestre, J.-C. Muñoz-Mateos, M. Seibert, T. Kim, E. Laurikainen, H. Salo, D. A. Gadotti, J. Laine, T. Mizusawa, L. Armus, E. Athanassoula, A. Bosma, R. J. Buta, P. Capak, T. H. Jarrett, D. M. Elmegreen, B. G. Elmegreen, J. H. Knapen, J. Koda, G. Helou, L. C. Ho, B. F. Madore, K. L. Masters, B. Mobasher, P. Ogle, C. Y. Peng, E. Schinnerer,

J. A. Surace, D. Zaritsky, S. Comerón, B. de Swardt, S. E. Meidt, M. Kasliwal, and M. Aravena. The Spitzer Survey of Stellar Structure in Galaxies (S4G). *PASP*, 122(898):1397, Dec. 2010. doi: 10.1086/657638.

S. K. Stuber, T. Saito, E. Schinnerer, E. Emsellem, M. Querejeta, T. G. Williams, A. T. Barnes, F. Bigiel, G. Blanc, D. A. Dale, K. Grasha, R. Klessen, J. M. D. Kruijssen, A. K. Leroy, S. Meidt, H.-A. Pan, E. Rosolowsky, A. Schruba, J. Sun, and A. Usero. Frequency and nature of central molecular outflows in nearby star-forming disk galaxies. *A&A*, 653:A172, Sept. 2021. doi: 10.1051/0004-6361/202141093.

J. Sun, A. K. Leroy, A. Schruba, E. Rosolowsky, A. Hughes, J. M. D. Kruijssen, S. Meidt, E. Schinnerer, G. A. Blanc, F. Bigiel, A. D. Bolatto, M. Chevance, B. Groves, C. N. Herrera, A. P. S. Hygate, J. Pety, M. Querejeta, A. Usero, and D. Utomo. Cloud-scale Molecular Gas Properties in 15 Nearby Galaxies. *ApJ*, 860 (2):172, June 2018. doi: 10.3847/1538-4357/aac326.

J. Sun, A. K. Leroy, E. Schinnerer, A. Hughes, E. Rosolowsky, M. Querejeta, A. Schruba, D. Liu, T. Saito, C. N. Herrera, C. Faesi, A. Usero, J. Pety, J. M. D. Kruijssen, E. C. Ostriker, F. Bigiel, G. A. Blanc, A. D. Bolatto, M. Boquien, M. Chevance, D. A. Dale, S. Deger, E. Emsellem, S. C. O. Glover, K. Grasha, B. Groves, J. Henshaw, M. J. Jimenez-Donaire, J. J. Kim, R. S. Klessen, K. Kreckel, J. C. Lee, S. Meidt, K. Sandstrom, A. E. Sardone, D. Utomo, and T. G. Williams. Molecular Gas Properties on Cloud Scales across the Local Star-forming Galaxy Population. *ApJL*, 901(1):L8, Sept. 2020. doi: 10.3847/2041-8213/abb3be.

J. Sun, A. K. Leroy, E. Rosolowsky, A. Hughes, E. Schinnerer, A. Schruba, E. W. Koch, G. A. Blanc, I.-D. Chiang, B. Groves, D. Liu, S. Meidt, H.-A. Pan, J. Pety,

M. Querejeta, T. Saito, K. Sandstrom, A. Sardone, A. Usero, D. Utomo, T. G. Williams, A. T. Barnes, S. M. Benincasa, F. Bigiel, A. D. Bolatto, M. Boquien, M. Chevance, D. A. Dale, S. Deger, E. Emsellem, S. C. O. Glover, K. Grasha, J. D. Henshaw, R. S. Klessen, K. Kreckel, J. M. D. Kruijssen, E. C. Ostriker, and D. A. Thilker. Molecular Cloud Populations in the Context of Their Host Galaxy Environments: A Multiwavelength Perspective. *AJ*, 164(2):43, Aug. 2022. doi: 10.3847/1538-3881/ac74bd.

M. P. Véron-Cetty and P. Véron. A catalogue of quasars and active nuclei: 13th edition. *A&A*, 518:A10, July 2010. doi: 10.1051/0004-6361/201014188.

C. D. Wilson, B. E. Warren, J. Irwin, J. H. Knapen, F. P. Israel, S. Serjeant, D. Attewell, G. J. Bendo, E. Brinks, H. M. Butner, D. L. Clements, J. Leech, H. E. Matthews, S. Mühle, A. M. J. Mortier, T. J. Parkin, G. Petitpas, B. K. Tan, R. P. J. Tilanus, A. Usero, M. Vaccari, P. van der Werf, T. Wiegert, and M. Zhu. The JCMT Nearby Galaxies Legacy Survey - IV. Velocity dispersions in the molecular interstellar medium in spiral galaxies. *MNRAS*, 410(3):1409–1422, Jan. 2011. doi: 10.1111/j.1365-2966.2010.17646.x.

E. L. Wright, P. R. M. Eisenhardt, A. K. Mainzer, M. E. Ressler, R. M. Cutri, T. Jarrett, J. D. Kirkpatrick, D. Padgett, R. S. McMillan, M. Skrutskie, S. A. Stanford, M. Cohen, R. G. Walker, J. C. Mather, D. Leisawitz, I. Gautier, Thomas N., I. McLean, D. Benford, C. J. Lonsdale, A. Blain, B. Mendez, W. R. Irace, V. Duval, F. Liu, D. Royer, I. Heinrichsen, J. Howard, M. Shannon, M. Kendall, A. L. Walsh, M. Larsen, J. G. Cardon, S. Schick, M. Schwalm, M. Abid, B. Fabinsky, L. Naes, and C.-W. Tsai. The Wide-field Infrared Survey Explorer (WISE): Mission

Description and Initial On-orbit Performance. *AJ*, 140(6):1868–1881, Dec. 2010. doi: 10.1088/0004-6256/140/6/1868.